Optical Diagnostics of Discharges in and in Contact With Liquids

Thiery Belmonte, Peter Bruggeman

Optical diagnostics of discharges in and in contact with liquids

Thiery Belmonte[1,*] and Peter Bruggeman[2,$]

[1]Institut Jean Lamour, CNRS and Université de Lorraine, 504011 Nancy, France

[2]Department of Mechanical Engineering, University of Minnesota, Minneapolis, MN 55455, U.S.A.

[*]thierry.belmonte@univ-lorraine.fr

[$]pbruggem@umn.edu

Keywords:

Discharges and liquids ; Optical diagnostics ; Plasma applications ; Plasma discharges

Graphical abstract:

Abstract:

Discharges in liquids have been the subject of intensive investigations for a broad range of applications and involve highly coupled and complex phenomena with timescales ranging from picoseconds to seconds and length scales from micrometers to centimeters. This review focuses on some of the challenges pertaining optical diagnostics of plasmas in and in contact with liquids this includes interpretation of optical emission spectra, the inherent stochastic nature of many discharge phenomena including the initial stages of plasma ignition and the large gradients in species and plasma properties interfacing with a dynamic liquid interface. We report recent notable advances, controversies in interpretations of diagnostics and remaining opportunities.

1. Introduction:

Discharges in liquids have been the subject of intensive investigations, as they involve highly coupled and complex phenomena with timescales ranging from picoseconds to seconds and length scales from micrometers to centimeters [1], [2], [3]. Determining the key plasma properties and species densities of such discharge phenomena can be a real challenge as available diagnostics are often limited, or their results are difficult to interpret. Optical emission spectroscopy is one of the simplest methods to implement and can provide essential information about the behavior of these ionized media. However, it is difficult to accurately interpret emission spectra because the spectra are made more complex by

the appearance of optically thick media, the dynamic changes of the plasma-liquid interface, the highly spatiotemporal dynamic ranges of the phenomena of interest and often resulting huge spatial gradients in species densities [1], [4], [5]. This is why having access to localized and dynamic information is crucial for comprehending evolving phenomena and elucidating underlying hypotheses.

Before interpreting emission spectra, it is generally necessary to grasp the primary mechanisms influencing the behavior of the surveyed environment, paradoxically mirroring what researchers endeavor to identify [6]. It is therefore important to have safeguards in place to define the limits of validity of a hypothesis likely to affect the general interpretation of an observation. It is also tricky to use concepts of equilibrium in non-equilibrium media or to postulate the existence of several phenomena when one can only describe the observable.

These limitations have recently led to significant efforts in complementing passive optical emission spectroscopy measurements with laser diagnostics, particularly for the measurement of reactive species densities [1], [7]. While laser diagnostics require often less assumptions and pre-knowledge of key plasma conditions and can allow for detailed spatiotemporal resolved measurements, laser diagnostics are typically no single shot measurements hence requiring the accumulation of signal over multiple reproducible discharge events. In the context of liquid discharges, obtaining such dynamic information is particularly complex due to inherent time lags during initiation and the ubiquitous formation of filaments which leads to inherent stochastic behavior that can only be statistically assessed.

This review focuses on some of the challenges pertaining optical diagnostics of plasmas in and in contact with liquids, reports related recent notable advances in the field and controversies in interpretations of diagnostics and remaining opportunities.

2. Discharge non-homogeneity, stochastic nature and plasma stabilization

In the field of plasmas in liquids, it is nearly always assumed that we are dealing with optical thin plasmas, nonetheless line broadening measurements suggest that the plasma densities are sometimes so high ([8] see also further) that this is not necessarily always the case and reabsorption of the emission can occur. In the case of an optical thick plasma, one might not only lose information from the high-density core of the plasma, but the interpretation of the emission becomes exceedingly complex and can only be in specific cases be achieved with easy techniques such as the Bartels method to analyze self-reversed emission lines [9]. While chemical models have assumed a two-zone plasma: a hot core and a colder surrounding plasma to be able to predict the plasma-induced chemistry by streamers in liquid water [10], such a first order approximation has not been implemented to analyze emission spectra to our knowledge.

In many applications-oriented studies, discharge intensities will significantly vary in space and time and typically studies are focused on optical emission spectroscopy which is an inherent line-integrated measurement technique and measurements will inherently be spatially or temporally averaged to some extent. Nonetheless, the information produced can be of significant value to obtain an overall idea of the plasma and process conditions, a detailed understanding of specific aspects of the underpinning plasma physics or plasma-liquid interactions often requires detailed spatially and temporally resolved measurements to resolve for example species gradients near the plasma-liquid interface. One of the very few reported examples of spatially resolved OES measurements in a streamer discharge in a liquid is shown in **Fig. 1**. While single shot laser diagnostics might become within reach for techniques such as electric field induced second harmonic generation (EFISH) and

Rayleigh scattering-based methods, in general emission and laser-based methods will require a highly reproducible discharge allowing for signal accumulation.

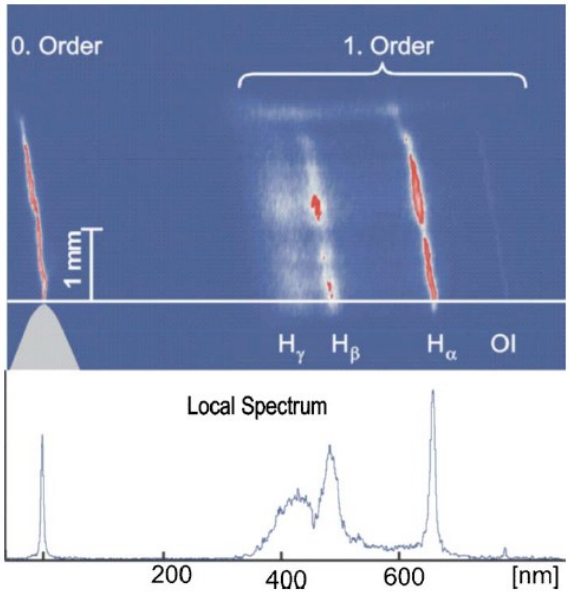

Figure 1 : - Spatially resolved line emission from a single secondary streamer in liquid water about 100 ns after streamer initiation obtained with an exposure time of 3 ns. The upper image shows changes in the emission profile along the streamer length. The bottom image shows a horizontal cut through the spectrum showing the ubiquitous H_α and H_β lines, and significantly higher order lines of the hydrogen Balmer series. Reproduced with permission from An *et al*. *[11]*.

In recent years, several groups have successfully worked on discharge stabilization for plasmas in and in contact with liquids. This includes the stable generation of bubbles by gas puffing [12], reproducible (vapor) bubble generation in a Hele-Shaw cell for emission [13] and the first laser induced fluorescence measurements [14], single droplet [15] or controlled droplet train generation [16] to study plasma-droplet interaction, a flowing liquid electrode with a steady concave surface enabling for a stable plasma-liquid surface unaffected by evaporation and allowing for high spatial resolution near interfacial laser diagnostics [17], [18] or a system of communicating vessels to achieve the same goal [7]. These stabilized discharges have enabled the measurement of selected plasma properties and species densities in a growing body of research that provides key insights in for example reactive species densities that are not easily measured using optical emission spectroscopy. **Fig. 2** shows an example of a stabilized pulsed discharge generated between a needle electrode and a solution interface generated by an overflowing solution from a tube. The continuously refreshing liquid combined with the convex interface allows long-duration measurements with a high spatial resolution up to ~30 µm near the plasma-liquid interface. More details of the use of laser diagnostics are discussed below after we discuss challenges and opportunities for optical emission spectroscopy in the next section.

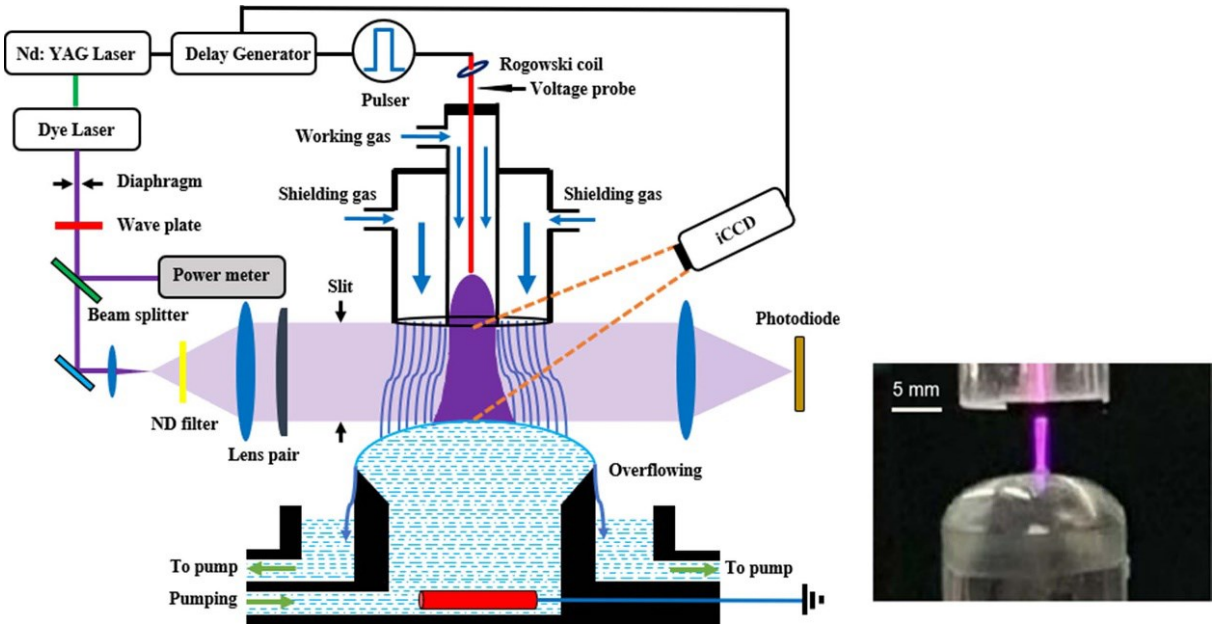

Figure 2. Schematic of setup with a tube with an overflowing solution which enables the generation of a highly stable plasma-liquid interface for many hours that is continuously refreshed to avoid rapid drift in solution properties. This approach has been shown to enable 2D planar laser induced fluorescence with a spatial resolution of 30 µm near a stable plasma-liquid interface. The inserted picture shows an image of a nanosecond pulsed glow discharge plasma impinging onto the flowing solution. Reproduced with permission from *[17]*.

3. Optical Emission Spectroscopy (OES)

In this section we review the use of optical emission spectroscopy with a focus on interrogating discharges in the dense liquid phase. We have organized this section aligned with the three main plasma emissions observed in plasmas: atomic line emission, molecular band emission and continuum radiation. Many works are devoted to this topic and for a review of the approaches the reader is referred to [19] for the fundamental background and references therein.

a. Atomic line broadening

Line broadening in plasmas is due to the interaction of the emitting atom with their environment and has been studied in detail. Line broadening has been extensively used to measure the gas temperature (utilizing Doppler or van der Waals broadening) [20], electron densities (and temperatures at time [21]) and recently even gas composition (Resonance broadening) [22]. The theories are well established for moderate gas and electron densities, but special treatments are needed at high pressures/neutral densities and electron densities that are the focus of this review.

i. Interaction potentials

While in many plasma studies, line broadening is analyzed with fitting line profiles with Gaussian, Lorentzian or Voigt profiles, in many cases this is not valid for plasmas in liquids and more advanced approaches are needed. In this section we briefly outline the origin of line broadening in the general context of force field interactions. The radiation emitted by an atom is influenced by the force field exerted by neighboring species. The pair consisting of the radiator and its perturber behaves as a molecular system. The force field arises from a potential energy difference, denoted as $\Delta\Phi$, measured in Joules. It can be expressed as the difference:

$$\Delta\Phi(r) = \Phi_{e'}(r) - \Phi_e(r) \quad (1)$$

where *e′* and *e* refer to the energy surfaces on which the interacting species approach the initial and final atomic states of the transition when $r \longrightarrow \infty$. Here, r denotes the internuclear distance between the radiator and the perturber. Typically, this potential energy conforms to a power law:

$$\Delta\Phi(r) = \pm\frac{\hbar C_p'}{r^p} = \pm\frac{C_p}{r^p} \tag{2}$$

where $\hbar$ is the reduced Plank constant and $C_p' = C_p/\hbar$ the potential constant expressed in $\mathrm{m}^p\ s^{-1}$. The parameter *p* takes the values of 2 for linear Stark, 4 for quadratic Stark, 3 for resonant, 6 for van der Waals and 6 and 12 for Lennard-Jones interactions.

However, certain interactions undergo more intricate processes that cannot be adequately described by functions of the previous type. For example, the presence of satellites in line transitions necessitates more precise potentials to replicate all the characteristics of the spectral lines. In this context, Anderson [23], [24] and Talman [25] formulated a theory of spectral line pressure broadening, where the profile is determined by the Fourier transform of an autocorrelation function of a unique dipole, denoted as φ, utilizing the relation:

$$I(\Delta\omega) = \frac{1}{\pi}\mathrm{Re}\left(\int_0^{+\infty}\left(\varphi(s)\right)^N e^{i\cdot\Delta\omega\cdot s}ds\right) \tag{3}$$

This expression assumes an additive pair-interaction from *N* perturbers $\left(\varphi(s)\right)^N$, thus neglecting the interperturber correlations. Additionally, it assumes that the electric-dipole moment during a collision is the same as it is for infinite separation of the emitting atom and its perturber. It is possible to demonstrate that:

$$\varphi(s) = \left(1 - \frac{V'(s)}{V}\right)^N \approx \exp\left(-\frac{N}{V}V'(s)\right) \tag{4}$$

where V is the volume that contains the *N* perturbers:

$$V = 2\pi\int_0^{\infty} b\cdot db\int_{-\infty}^{+\infty} dx_0 \tag{5}$$

x_0 is the position of the perturber at the beginning of the time-interval 0 to s along the straight line of impact parameter *b* (see **Fig. 3a**). $V'(s)$ represents the collision volume defined by:

$$V'(s) = 2\pi\int_0^{\infty} b\cdot db\int_{-\infty}^{+\infty} dx_0 \times\left\{1 - \exp\left[i\int_0^s \nu([(x_0+ut)^2 + b^2]^{0.5})dt\right]\right\} \tag{6}$$

where ν is the frequency at the considered time and u is the velocity of the perturber. **Eqs (3)**, **(4)** and **(6)** lead to the so-called impact and quasi-static approximations in the proper limits. The assumption of the *impact theory* is that the collisions are short compared to the time between them. The *quasi-static theory* is valid if the frequency perturbation for a given atom can be written as the sum of that due to all others in the gas.

Allard *et al*. [26] proposed a *unified theory* demonstrating how equation (6) must be modified to include the effect of the variation of electric-dipole moments on the shape of pressure-broadened atomic spectral lines. This approach accurately describes the experimental profile from the line center to the far line wings. For a transition α = (*i*, *f*) from an initial state *i* to a final state *f*, with the notation of **Eq.(1)**, one has:

$$V'_{\alpha}(s) = \frac{1}{\sum_{e,e'}^{(\alpha)}|d_{ee'}|^2}\sum_{e,e'}^{(\alpha)}\int_0^{+\infty} 2\pi b db\int_{-\infty}^{+\infty} dx\,\tilde{d}_{ee'}[r(0)]\left[\exp\left(\frac{i}{\hbar}\int_0^s \Delta\Phi[r(t)]\,dt\right)\tilde{d}_{e'e}[r(s)] - \tilde{d}_{ee'}[r(0)]\right] \tag{7}$$

where $\tilde{d}_{ee'}[r] = d_{ee'}(r)\exp\left(-\frac{\Phi_e(r)}{2kT}\right)$ can be defined as a *modulated* dipole, $d_{ee'}(r)$ being the radiative dipole transition moment. Allard *et al*. [27] were the first to successfully reproduce the He-He collisional profiles arising from the triplet 2p–3s transitions using a unified line-shape semiclassical

theory. This theory utilizes the *ab initio* molecular potentials given in **Fig. 3c** (the unperturbed He(3 ^{3}S)-He(2 ^{3}P) line lies at 706.69 nm). It's noteworthy that the central part of the line's shape can be effectively fitted by a Lorentzian profile, consistent with the pressure broadening theory based on the impact approximation. The remarkable agreement observed in **Fig. 3b** between experimental and theoretical data for the near wing of the line profiles, which include multiple blue satellites, confirms the accuracy of the interaction potentials. All aspects are accurately reproduced up to a density of approximately 8×10^{20} cm^{-3}. Beyond this threshold, all theories fail to predict the evolution of the line width (**Fig. 3d**).

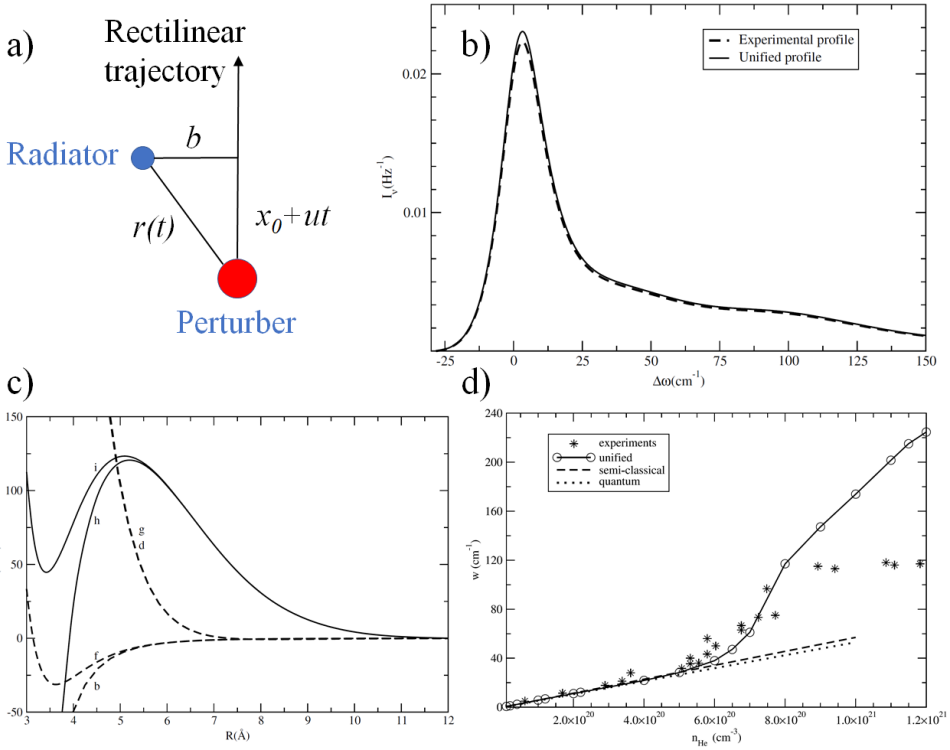

Figure 3: a) Schematic illustrating the collisional parameters required for the unified theory. b) Experimental profile of the He(3 ^{3}S)-He(2 ^{3}P) transition at a pressure of 1.6 MPa and a temperature of 300 K, (n_{He} = 3.8 × 10^{20} cm^{-3}), compared to the theoretical profile obtained from the unified theory. Reproduced with permission from [28]. c) Potential energies determined by *ab initio* calculation for the triplet 3s (full line) and 2p (dashed line) states of the He_2 molecule. Considered He_2^* transitions are: $3s\ h\ ^3\Sigma_u^+ \rightarrow 2p\ b\ ^3\Pi_g$, $3s\ i\ ^3\Sigma_g^+ \rightarrow 2p\ f\ ^3\Pi_u$, $3s\ h\ ^3\Sigma_u^+ \rightarrow 2p\ g\ ^3\Sigma_g^+$ and $3s\ i\ ^3\Sigma_g^+ \rightarrow 2p\ d\ ^3\Sigma_u^+$. Reproduced with permission from [29]. d) Variation of the width in the He density range 0.1 to 12 × 10^{20} cm^{-3} for 300 K (for comparison, the liquid density at 4.2 K is 2 × 10^{22} cm^{-3}). The impact values and experimental determinations are reported. Reproduced with permission from [29] and [30].

ii. Cryogenic discharges

The broadening and shift of the line emitted in cryogenic helium, such as in liquid and dense gas, markedly differs from the line emitted in gaseous helium at high temperature and pressure. Both lines exhibit asymmetric shapes, but in cryogenic helium, the prominence of the blue wing is significantly greater. Additionally, the blue shift observed in cryogenic helium is substantially larger (**Fig. 4**).

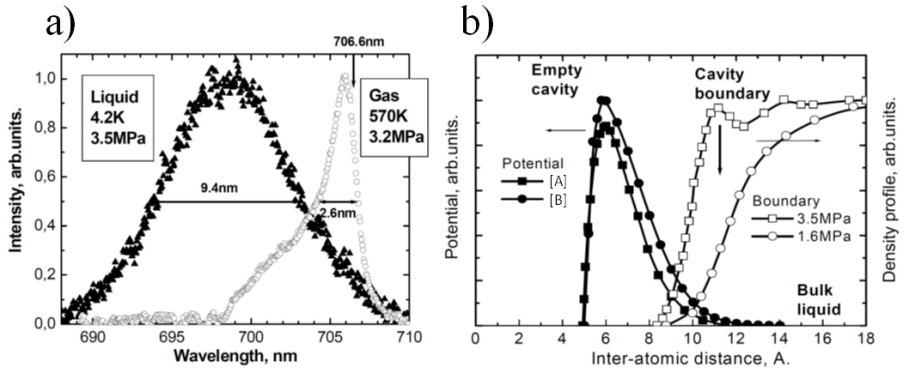

Figure 4: a) Comparison of the He(3 ^{3}S)-He(2 ^{3}P) transition observed in liquid He at 4.2K and in gaseous He at 570 K under the same pressure 3.5 MPa [31]. b) Calculated He*-He potentials (a) is taken from [29] and b) from [32]) as a function of the distance between atoms (lines with full symbols, left axis). *Ab initio* methods were used to calculate these potentials with the MOLPRO software. Density profile of a cavity (or bubble, see text) boundary (lines with empty symbols, right axis). Reproduced with permission from [31].

The occurrence of "bubbles" (distinct from bubbles commonly found in liquids) or "cavities" that surround the radiators, *i.e.* excited helium atoms, was initially observed in superfluid Helium II, occurring below the superfluid transition temperature of 2.17 K, and subsequently observed up to temperatures of 20 K [33], [34]. Essentially, the repulsive Pauli exchange interaction between the Rydberg electrons of He^* and He_2^* excited states and the surrounding closed-shell helium atoms creates a void ranging from 7 to 15 Å in size. This void is slightly smaller than the free electron's void size in the liquid, which measures 18.5 Å [35].

The theoretical treatment of such an interaction is described in several works [36], [37], [38]. In the density functional theory used to account for this interaction, the time-dependent Schrödinger-like equation is solved [39]:

$$i\hbar\frac{d\psi}{dt} = -\frac{\hbar^2}{2m}\nabla^2\psi + V_{DFT}[\psi]\psi \tag{8}$$

where $V_{DFT}[\psi]$ is a non-local functional of ψ. It uses the Dalfovo-Stringari functional [40], which is the sum of short range correlation and a screened pair potential that includes terms related to kinetic many-body effects.

The solution for the ground state can be obtained using the imaginary time-step method [41], whereas the real time dynamics results from **Eq. 8**. [42].

iii. The specific case of H I lines

Hydrogen lines are ubiquitous in discharges produced in liquid water and hydrocarbons that are often used. Hence, hydrogen lines deserve special attention in the context of plasmas in liquid. The standard theory of Stark-broadened profiles of hydrogen lines is formulated under the quasistatic approximation for ions and the impact binary approximation for electrons [43], [44]. The highly mobile electrons induce sudden phase variations in the emitted wave, while the heavier and slower ions create electric fields that remain relatively constant over the typical emission duration. Due to the light mass of hydrogen, the contribution of electrons to the phenomenon cannot be overlooked. As previously discussed, Gigosos and Cardeñoso [45] employed the autocorrelation function of the atomic dipole momentum, obtained through a Fourier transform of its average across a specific statistical ensemble, to derive the profile of the selected line. Their modeling approach relies on the determination of the mean interparticle distance divided by the Debye radius and the reduced mass of the radiator–perturber pair. Subsequently, microfield time sequences of ions and electrons are

generated and appropriately overlapped. For each electron density / temperature pair (n_e, T), the set of differential equations governing the time evolution of the autocorrelation function is integrated.

These researchers were able to generate profile data for Balmer and Lyman α, β and γ transitions with density values ranging from 10^{14} cm^{-3} to $10^{18.67}$ cm^{-3}, temperatures ranging from 0.19 to 19.4 eV and reduced masses of the radiator–perturber pair ranging from 0.5 to 2.0.

The H_β transition of the Balmer series is characterized by the presence of a central dip under certain conditions as shown in **Fig. 5a**. As previously explained, this dip is unrelated to the optical thickness of the medium. The amplitude of the dip, expressed as ($I_{max} - I_0$) / I_{max} in percentage, is depicted in **Fig. 5b**. The dip becomes more pronounced when the reduced mass μ, defined between the radiator and the collider, increases, and conversely, as the electron density increases.

Two remarks must be made. First, the variation of the central dip is not smooth as a function of the electron density and the reduced mass of the radiator-collider pair (**Fig.5b**). Second, it is not symmetric in wavelength and its shape depends on the electron density [46]. Consequently, the asymmetric shape of the H_β line must be described by many parameters [47].

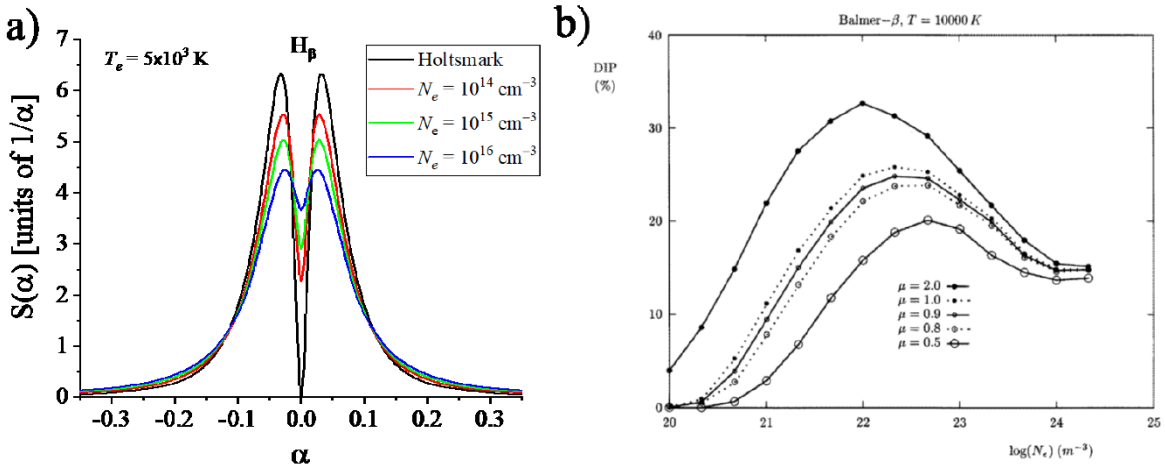

Figure 5: a) Evolution of the shape of the H_β transition at 486.13 nm and 5,000 K as historically predicted by Griem *et al*. [48] and comparison with the Holtsmark profile. Here, $\alpha = \Delta\lambda / F_0$, where $\Delta\lambda$ and F_0 are the wavelength separation from the unperturbed line of wavelength λ, and the Holtsmark field strength. Note that the dip in this case decreases with the electron density in the range 10^{20}-10^{22} m^{-3}. b) Central dip, expressed in %, as a function of the electron density for different values of the reduced mass, showing evolutions that were not predicted by the first Griem's model. T = 10,000 K in all cases [45].

Practical expressions can be used to determine the electron density, which filter out the dependence on T and μ [49]:

$$FWHA\,[H_\alpha] = 0.549\ \text{nm} \times \left(\frac{n_e}{10^{17}\ \text{cm}^{-3}}\right)^{0.67965}$$

$$\begin{cases} FWHA\,[H_\beta] = 1.666\ \text{nm} \times \left(\frac{n_e}{10^{17}\ \text{cm}^{-3}}\right)^{0.68777} \\ FWHM\,[H_\beta] = 4.800\ \text{nm} \times \left(\frac{n_e}{10^{17}\ \text{cm}^{-3}}\right)^{0.68116} \end{cases}$$

$$FWHA\,[H_\gamma] = 2.433\ \text{nm} \times \left(\frac{n_e}{10^{17}\ \text{cm}^{-3}}\right)^{0.68575}$$

where FWHA is the Full Width at Half Area and FWHM is the Full Width at Half Maximum of the selected line. The shift of the H_α central wavelength can be approximated, between 13,000 and 20,000 K, by [50]:

$$n_e \text{ cm}^{-3} = 10^{17} \times \left(1.359 + 2.0757 \times \Delta\lambda_0 \text{ Å} + 0.0037 \times \Delta\lambda_0^2 \text{ Å}^2\right)$$

For the H_β transition, it is preferable to utilize the separation $\Delta\lambda_{SP}$ between the 2 peak maxima on each side of the central dip [51]:

$$\begin{cases} \log n_e \text{ m}^{-3} = 22.621 + 1.452 \log \Delta\lambda_{SP} \text{ nm for } \mu \leq 2 \\ \log n_e \text{ m}^{-3} = 22.661 + 1.416 \log \Delta\lambda_{SP} \text{ nm for } \mu = 0.5 \end{cases}$$

iv. Asymmetric line profiles

It is possible to estimate the electron density in discharges in liquids close to the LTE by exploiting the asymmetry of some transitions caused by Stark broadening. Under these conditions, Saha's equation can be used to estimate the density of electrons and ions.

Optical transitions in spark discharges in liquids are broadened by several phenomena whose relative weight changes with time due to the rapid evolution of the main parameters controlling the discharge. The electron temperature, the electron density, the total pressure and the medium optical thickness are known to vary strongly at the very beginning of the process, *i.e.* from the first few 10s of ns. If the ion density is high enough, the lines can be asymmetrically broadened.

Stark profiles are produced under the action of high frequency electron fields (the linear Stark effect obeying a potential $\Delta V_2 = -\hbar C_2/r^2$) and under the action of low-frequency ion fields (the quadratic Stark effect with $\Delta V_4 = -\hbar C_4/r^4$). In the case of a non-hydrogenoid atomic transition, the ion broadening is not negligible, and the line profiles become asymmetric.

Methods based on the so-called 'six free parameters deconvolution' (SFPD) procedure have been developed to determine the parameters of given emission lines from experimental data [52], [53], [54]. In the quasi-static approximation, the line profile is given by:

$$j_{A,R}(x) = \frac{1}{\pi} \int_0^\infty \frac{H_R(\beta)}{1+\left(x - A^{4/3}\beta^2\right)^2} d\beta, \tag{9}$$

where $x = \frac{\lambda - \lambda_0 - d_e}{w_e}$, w_e is the half width at half maximum (HWHM) of the Stark broadening due to electron collision and d_e is the corresponding Stark shift. $H_R(\beta)$ is the microfield intensity distribution function, which depends on the normalized intensity of the Holtsmark field $\beta = F / F_0$, F_0 being the intensity of the Holtsmark field. A is the broadening parameter due to static ions. R is the ratio of the average distance between the ions and the Debye radius, *i.e.* the Debye screening parameter:

$$R = \left[\frac{36\pi e^6 n_e}{(k_B T_e)^3}\right]^{1/6} \approx 0.0899 \frac{\left(n_e[\text{cm}^{-3}]\right)^{1/6}}{T_e^{1/2}}. \tag{10}$$

The expression of $j_{A,R}(x)$ is determined thanks to the Woltz tables [55] from w_e. When the ion dynamics is no longer negligible, it is necessary to introduce a correction factor. The criterion to be fulfilled is then [52]:

$$B = A^{1/3} \frac{8.06\times10^{-7} w_e^{ref}[nm]}{(\lambda[nm])^2} \left(n_e[m^{-3}]\right)^{2/3} \sqrt{\frac{\mu[amu]}{T_g[K]}} < 1, \tag{11}$$

where w_e^{ref} is the value of w_e when $n_e = 10^{23}$ m^{-3}. μ is the reduced mass of the ion or neutral perturber in arbitrary mass units. This means that strong collisions due to electrons and ions are well separated in time. The total broadening is then given by:

$$\Delta\lambda_s = 2w_e\left[1 + 1.75AD_J(1 - 0.75\kappa R)\right] \quad (12)$$

with $D_J = \frac{1.36}{1.75(1-0.75R)}B^{-1/3}$ if $B < \left(\frac{1.36}{1.75(1-0.75R)}\right)^3$ or $D_J = 1$ if $B \geq \left(\frac{1.36}{1.75(1-0.75R)}\right)^3$ [52]. In the latter case, ion dynamics are negligible, and the line shape is treated by considering the quasi-static approximation. This approach must also include an optical model to account for the optical thickness of the medium [19].

It is often used to analyze discharges in liquids acting as nanoparticle generators, since high currents are usually required (tens of amperes between metallic electrodes of millimeter or sub-millimeter radius, leading to huge current densities required for metal erosion). Burakov *et al*. [56] used Cu I lines resulting from plasma erosion of copper electrodes to determine electron densities around 3 × 10^{16} cm^{-3} for a discharge produced by a spark generator reaching up to 80 A in water or ethanol. Belmonte *et al.* [57], [58] recorded time-resolved asymmetric emission lines for discharges generated between two zinc [57] and two bismuth [58] electrodes. In **Fig. 6**, the time evolution of the shape of the three zinc lines around 475 nm and one bismuth line at 412.17 nm emitted in liquid nitrogen is plotted from times after ignition ranging from 200 to 950 ns. The asymmetric profile of the lines, with strongly broadened red wings, gives an estimate of the electron density, which varies by an order of magnitude over the time period.

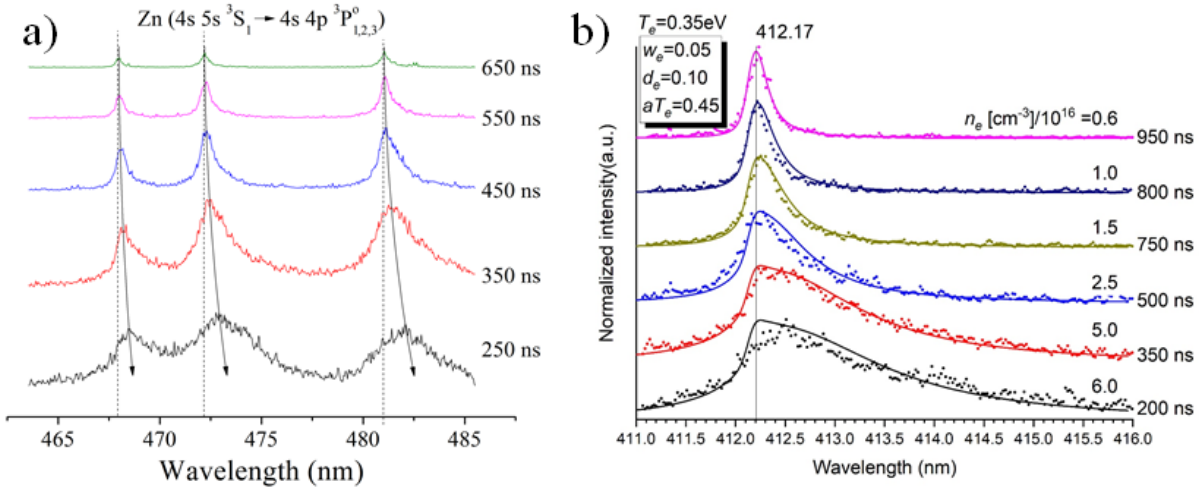

Figure 6: a) Time evolution of the three zinc lines observed between 465 and 485 nm between 250 and 650 ns. Reproduced with permission from [57]. The electron density varies from 5.5 × 10^{16} cm^{-3} to 1.5 × 10^{15} cm^{-3}. T_e ~ 0.45 eV. P = 8 bars. b) Normalized intensity of the emission of the transition at 412.17 nm as a function of time. Stark parameters are given in the inset. T_e = 0.35 eV. P = 5 bars. Instrumental broadening is 100 pm. Stark broadening is 850 pm. The sum of all other contributions is less than 10 pm. Reproduced with permission from [58].

A. von Keudell *et al*. [59] produced discharges in distilled water with applied voltages of 20 kV and pulse lengths of 10 ns applied to a tungsten tip of 50 µm diameter. The current was estimated to be around 10 A. The emission lines of the blue-broadened H_α transition were recorded from the ionization region. From Stark broadening, they determined electron densities up to 5 ×10^{19} cm^{-3} and electron temperatures around 6-7,000 K. Similar results were obtained by Namihara *et al*. [60] with a magnetic pulse compressor delivering 40 J/pulse at 3.5-kV charging voltage, although they used a Lorentzian function to fit asymmetric profiles. They found electron densities higher than 10^{18} cm^{-3} consistent with the seminal work of Sunka for microsecond pulsed discharges [8]. At such high electron densities (>10^{18} cm^{-3}), the ideal character of the plasma can be questioned [61].

v. Lack of atomic emission lines and non-ideal plasma

The plasma parameter, Λ, is the argument of the Coulomb logarithm, which is the ratio of the maximum impact parameter to the classical distance of closest approach in Coulomb scattering:

$$\Lambda = 4\pi \left(\frac{\varepsilon_0 k_B}{e^2}\right)^{3/2} \times \sqrt{\frac{T_e^3}{n_e}} \approx 4.13 \times 10^6 \sqrt{\frac{T_e^3}{n_e}} \tag{13}$$

where ε_0 is the permittivity of free space, k_B the Boltzmann constant, and e the electron charge. An ideal plasma requires that $\Lambda \gg 1$. Taking $\Lambda = 10$ and T_e = 11,604 K, we get $n_e < 3 \times 10^{17}$ cm^{-3}. For $\Lambda \approx 1$, *i.e.* $n_e \approx 3 \times 10^{18}$ cm^{-3}, the discharge is slightly non-ideal. Descoeudres *et al*. [62] used the closely related parameter Γ, which is the plasma coupling parameter, defined as a ratio of the Coulomb energy to the thermal energy:

$$\Gamma = \frac{e^2}{4\pi\varepsilon_0 k_B T_e} \times \sqrt[3]{\frac{4\pi n_e}{3}} = \frac{1}{3^{1/3}} \times \frac{e^2}{(4\pi)^{2/3}\varepsilon_0 k_B} \times \sqrt[3]{\frac{n_e}{T_e^3}} \approx \Lambda^{-2/3} \tag{14}$$

In the electrical discharge machining process, they could reach electron densities as high as $n_e \approx 2.5 \times 10^{18}$ cm^{-3}, which classifies these discharges as weakly non-ideal plasmas.

Since non-ideal plasmas are dense, a strong Stark broadening and shift of the spectral lines is naturally a characteristic sign of non-ideality. The dynamic microfields deform the energy spectrum of radiating atomic particles, *i.e.* they perturb the initial and final states of radiative transitions [63]. The atomic levels are shifted and split, resulting in line broadening and shift [64], [65] but also in the appearance of satellite peaks. This effect can be clearly observed in the optical spectra emitted by EDM plasmas, especially on the H_α line (**Fig. 7**). These effects are analogous to those previously presented for the appearance of satellites in pressure broadened He I transitions, but here caused by the Stark effect.

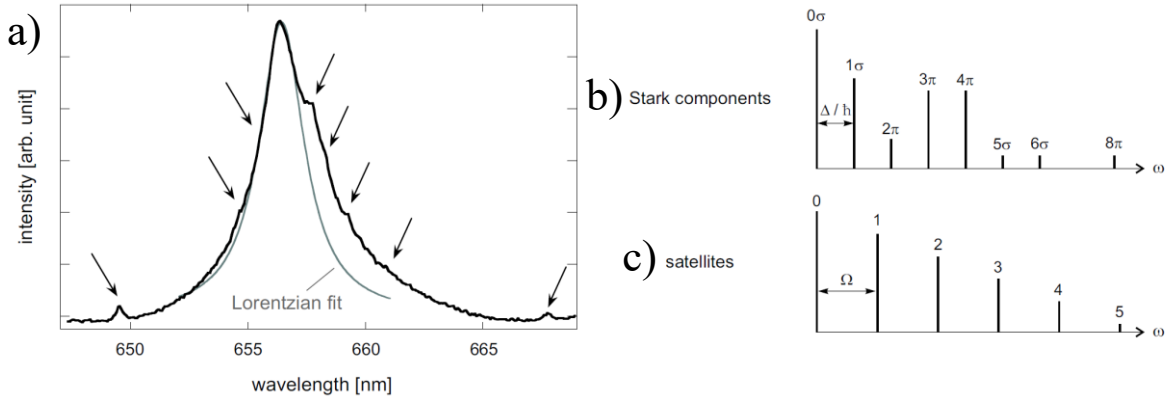

Figure 7: Complex structure of the H_α line in the EDM process for a weakly non-ideal discharge. Theoretical structure of the H_α line in a non-ideal plasma according to [66]: (a) Stark components of H_α; (b) satellite lines due to plasma waves or turbulence. The frequency $\omega = 0$ corresponds to the unperturbed H_α position (λ_0 = 656.28 nm). The components on the other side of the line are symmetrically positioned. Reproduced with permission from [67].

The absence of the H_β transition in spectra where such a line is obviously not obscured by other lines or buried in the background emission is due to the lowering of the ionization energy of the hydrogen atom. Both temperature and pressure can affect the partition function. This lowering can be estimated using the Debye–Hückel theory. This theory is also used to determine the energy of possible missing levels in a distribution.

The Ritz–Rydberg distribution is given by:

$$\mathrm{E}_p = \mathrm{E}_i - \frac{Ry}{\left(p + C_1 + \frac{C_2}{p^2}\right)^2} \text{ with } p < p_{\max} \tag{15}$$

where E_i is the ionization energy, *Ry*, the Rydberg constant, *p* the principal quantum number and C_1 and C_2 are two constants. Here, p_{max} is the number whose Ritz–Rydberg's energy is less than the ionization energy corrected by ΔE^{ion} due to charged particle effects:

$$\Delta E^{ion} = \frac{ze^2}{4\pi\varepsilon_0\lambda_D} \tag{16}$$

z is the effective charge number. λ_D is the Debye length. Taking z = 1, T_e = 11,604 K and $n_e = 2 \times 10^{19}$ cm^{-3}, we find $\Delta E^{ion} = 0.866$ eV, which is slightly higher than the energy required to suppress the *n* = 4 level (0.848 eV) and thus, the H_β transition.

We note that the electron density determined by Descoeudres *et al.* of 2.5×10^{18} cm^{-3}, is about an order of magnitude lower than this estimate, which is not negligible. We also note that with electron densities higher than 2×10^{19} cm^{-3}, Keudell *et al*. [59] should not observe the H_β transition, which they do. Further studies are then needed to clarify the behavior of discharges in liquids at very high electron densities. Although this could also be an indication that actual electron densities are lower and the assumption that the broadened line be dominated due to the Stark effect needs to be revisited.

vi. Case study: PEO process

We describe how some of the previously outlined methods can be applied to plasma electrolytic oxidation (PEO) treatments which convert the surface of a valve metal or alloy into an oxide layer. The choice for PEO as a case study is its exceeding complex and dynamic behavior together with the high electron densities. Typically, these PEO treatments are accomplished using high voltage, low frequency (around 50 Hz) AC supply in dilute alkaline electrolytes. The oxide layers obtained through PEO processing are thick, hard, and firmly adherent to the substrate. The formation of PEO coatings is a complex process involving three simultaneous operations: electrochemical reactions, plasma chemical reactions, and thermal oxygen diffusion reactions. The coatings resulting from these reactions typically consist of three-layer structures, including a porous outer layer, a dense intermediate layer, and a thin inner dense layer.

Light analysis is intricate as light emission depends on various factors. Each discharge generated penetrates into the substrate surface and traverses one or several of the aforementioned three layers. Consequently, light emission varies depending on the emissive region of the discharge, given the significant gradients that exist (refer to **Figs 8a1** to **8f1**). Discharge characteristics also undergo changes throughout the process (refer to **Figs 8a2** to **8e2**), and the emitted light likewise varies with the process time. Several stages have been proposed to account for this evolution, as depicted in **Figs 8a3** to **8d3**.

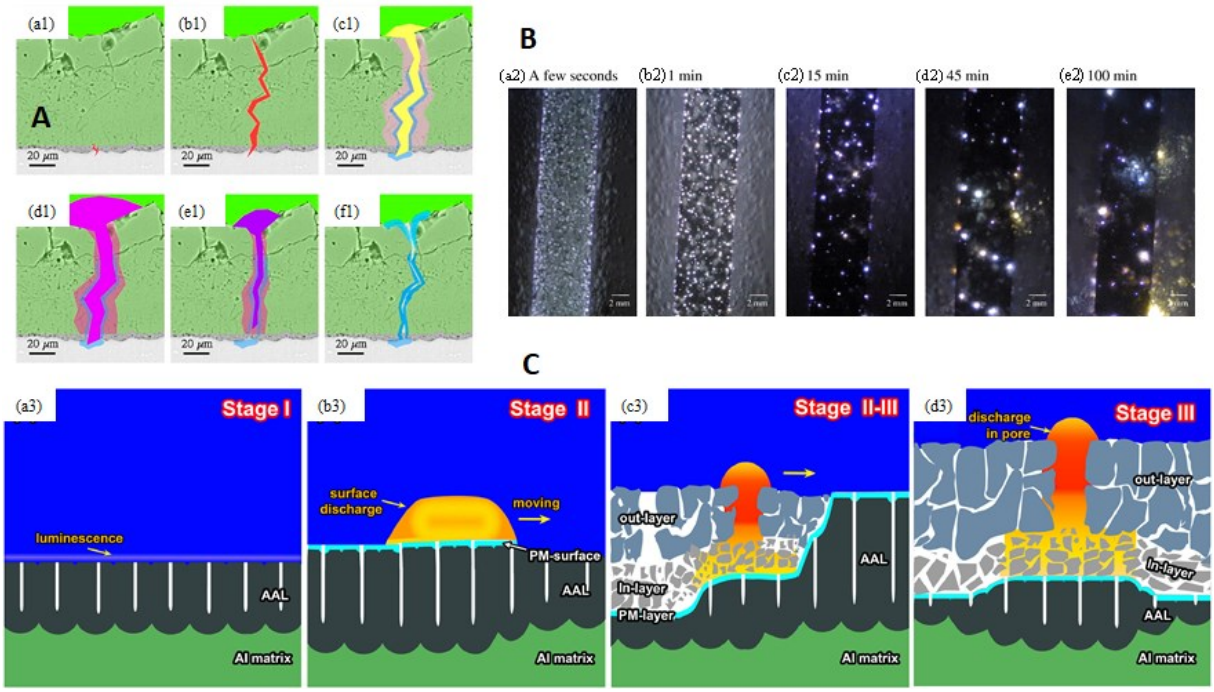

Figure 8: **A**: Schematic depiction of the sequence of events during a single discharge, showing: (a1) initial electrical breakdown, (b1) development of the plasma channel through the coating thickness, (c1) initial bubble growth and formation of oxide in the plasma, (d1) bubble expansion and heating of region around discharge, (e1) shrinkage and cooling as the plasma resistance rises, causing the current to fall, and (f1) final quenching and expulsion of some liquefied oxide from the channel. Reproduced with permission from [68]. **B**: Side-view pictures of aluminium alloy samples at different times of the PEO process from a few seconds (a2) to 100 min (e2). Reproduced with permission from [69]. **C**: Schematic diagrams illustrating the growth mechanism of the PEO coating in (a3) Stage I with uniform growth, (b3) Stage II with the growth localized under the moving surface discharges and the formation of the PM-surface, (c3) Stage II,III and (d3) Stage III. Reproduced with permission from [70].

Indeed, Dunleavy *et al*. [71] demonstrated that plasma emission spectra suggest the existence of two distinct regions: a central core characterized by high temperature (~16,000 ± 3500 K), with a high electron density (n_e ~5 × 10^{17} cm^{-3}), and a peripheral region, probably extending into the surrounding electrolyte, which is considerably cooler (~3000–4000 K) and less dense (n_e ~10^{15} cm^{-3}).

In the case of titanium processed by PEO, Aliofkhazraei *et al*. [72] classified OES signals into three different types (A, B, and C) based on their intensity and origin. Type B signals occur when the anodic material evaporates and are characterized by electron temperatures higher than 9,000 K. The A and C type signals result from gas discharges at the surface and in the pores of the oxide film, respectively. They occur during the initial stages of unipolar current treatments. The discharges are influenced by the ratio of anodic to cathodic current, the pulse duration and the type of electrolyte.

Liu *et al*. [73] identified two discharge modes: one with small spark size and another with large spark size. The latter only appears in the intermediate stage of the PEO process. The electron temperature in the plasma discharge zone ranges from about 3000 to 7000 K, and it appears to be influenced by the large discharges. The electron density remains in a relatively narrow range, from 8.5 × 10^{15} cm^{-3} to 2.6 × 10^{16} cm^{-3}.

Wang *et al*. [74] also determined the electron temperature by analyzing with the Boltzmann plot method H line data and obtained values in the range 6,000 to 30,000 K during the process. Hussein *et al*. [75] measured an electron density from the H_β transition around 2 × 10^{16} cm^{-3}.

Cheng *et al*. [76] provided estimates of the electron temperature in the case of a brass alloy, ranging from 4,400 and 7,000 K, using Boltzmann's plot and selecting only 5 Cu I lines. They observed that lines in the UV region had to be disregarded for consistency, leading to unrealistic temperatures values around 100 kK. They suggest that this discrepancy could be attributed to a lower detection efficiency of the spectrometer or self-absorption of the lines. They also proposed that the discharge structure comprises a hot core and a colder boundary. However, even with a core temperature around 10,000 K, the values remained far from estimates. Electron temperatures determined from the relative intensities of the lines of Cu, Zn, and H yielded more consistent values of approximately 6,800, 4,400 and 5,700 K, respectively.

Stojadinović *et al*. suggested in several works [77], [78], [79], [80], the existence of two and even three electron distributions corresponding to as many discharges in the plasma electrolytic process (PEO). Two populations of electron densities are estimated by fitting two Lorentzian profiles to the H_α and H_β line profiles. The third distribution is given by the fitting of another metallic line observed in the process. Electron densities are found to be close to a few 10^{15}, 10^{16} and 10^{17} cm^{-3} (refer to **Table 1**).

Table 1: Comparison between different estimations of the electron densities and temperatures made in selected reference works.

Reference	Material	Voltage/current	Lines	Electron densities	T_{exc}
[77]	Aluminium	50 mA cm^{-2}	H_α	0.8×10^{15} cm^{-3}	~3,300 K from W I*
				2.5×10^{16} cm^{-3}	40,000-45,000 K from O II
			Al II	0.6×10^{17} cm^{-3}	
[78]	Tantalum	450-550 V	H_β	0.9×10^{15} cm^{-3}	
		70 mA cm^{-2}		2.2×10^{16} cm^{-3}	
[79]	Titanium	400-450 V	H_β	3.8×10^{15} cm^{-3}	3,700 ± 500 K
		200 mA cm^{-2}		4.5×10^{16} cm^{-3}	
[81]	Magnesium -aluminium alloys	350-450 V	H_β	1.2×10^{15} cm^{-3}	4,000 K from Mg I
		100 mA cm^{-2}		2.3×10^{16} cm^{-3}	33,000 K from O II
			Al II / Mg II	(1-2) × 10^{17} cm^{-3}	
[75]	Titanium alloy (TA6V)	Uni / bipolar	H_β	~2×10^{16} cm^{-3}	3,500–9,000 K unipolar
		170 mA cm^{-2}			3,500–6,000 K bipolar
[71]	Aluminium alloy	150 mA cm^{-2}	H_β	~1×10^{15} cm^{-3}	3,000-4,000 K
			Si II / Mg II	5.0×10^{17} cm^{-3}	16,000 K
[73]	Aluminium alloy	100 mA cm^{-2}	H_β	0.85-2.60 × 10^{16} cm^{-3}	3,000-7,000 K from Al I

* sodium–tungstate was used as electrolyte

As previously discussed, the occurrence of multiple electron distributions in the PEO process is common, although it remains unclear whether they arise from multiple discharges and/or from distinct emission areas within discharges. This difficulty primarily stems from the inability to obtain time-resolved measurements of the light emitted by discharges in this particular process.

The selection of transitions is crucial, as certain lines may exhibit optical thickness. As explained by Stojadinović *et al*. [78], H_α self-absorption gives higher values of the electron density than the H_β profile when this latter is less self-absorbed. If the H_β transition is optically thin, then the estimated electron density is considered accurate.

Using two Lorentzian functions to fit the H emission lines can be misleading under these conditions. As illustrated in **Fig. 9**, there is not always a necessity to employ two distributions to achieve a satisfactory fit of experimental data, as the shape of the hydrogen line adopts a specific shape, as calculated by Griem [82] and improved next [45]. Utilizing the appropriate shape leads to a single value of the electron density in this scenario.

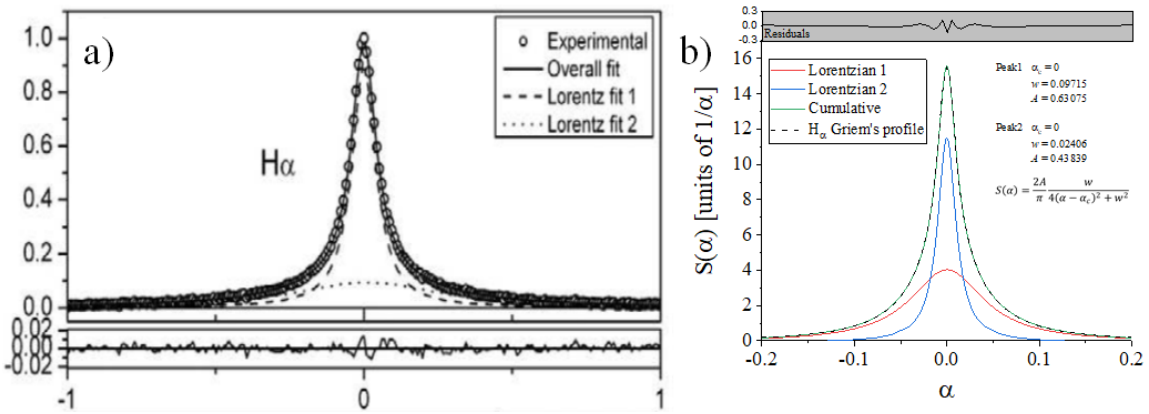

Figure 9: a) H_α emission line fitted with two Lorentzian. Reproduced with permission from [77]. b) Comparison between a single shape function given by Griem in [82] and two Lorentzian profiles.

Another important aspect concerns the reliability of the Boltzmann plot method in the PEO process. Firstly, it is important to note that the electron excitation temperature T_{exc} may not always accurately represent the electron temperature T_e. For these temperatures to be equivalent, it is necessary that energy levels are populated in accordance with the Boltzmann equilibrium distribution. This assumption holds true if local thermal equilibrium (LTE) is either complete or partial. In case of partial LTE, the upper energy level of the spectral line used for Boltzmann plot must exceed the lowest level determined by the pLTE condition. This condition expresses that the electron density required for the p^{th} level to be in equilibrium with the higher levels and the continuum, *i.e*. to have pLTE above level p, is given by:

$$n_e\ (\mathrm{cm}^{-3}) \geq 7.351 \times 10^{18} \frac{z^7}{p^{8.5}} \left(\frac{k_B T_e}{z^2 E_H^i}\right)^{1/2} \tag{17}$$

where p is the principal quantum number of the lowest level included in the partial LTE and z the effective charge seen by the bound electron. E_H^i is the ionization energy of the hydrogen atom.

It is essential to recognize that this lowest level will differ from one emissive species to another, because of differences in the absolute energy levels of each molecule.

Jovović *et al.* [77] evaluated with this criterion that for T_e = 1 eV and for W I lines, the pLTE condition is satisfied above $n_e = 5.5 \times 10^{15}$ cm^{-3}. For the same temperature but for O II lines, pLTE condition is satisfied above $n_e = 1.1 \times 10^{16}$ cm^{-3}. Since they determined three electron densities in their discharges

(0.8×10^{15} cm^{-3}, 2.5×10^{16} cm^{-3}, 0.6×10^{17} cm^{-3}), the hypothesis of pLTE may or may not be valid depending on the region where the light originates from. From the results in **Table 1**, we observe that ionic lines always give higher electron density values. This is probably due to the region where emissions occur, with metals evaporating in the hotter region of the discharge. As it is also the case for O II lines, we infer that it is possible because the inward flux of water to the plasma core is accompanied by a progressive dissociation of the molecule until it reaches this region where O atoms can finally be ionized and excited.

b. Molecular emission

Gas phase plasmas typically have an abundance of molecular emission. Diatomic ro-vibrational bands have been extensively used to determine rotational temperatures which are typically representative for the gas temperature although many cases occur for which the interpretation of ro-vibrational systems are more complex, including plasmas in and in contact with liquids.

i. Non-equilibrium ro-vibrational distributions

Many ro-vibrational spectra can be observed in the visual spectral range. In this spectra range, emission originates from electronically excited states. If these states are produced by electron impact excitation, the resulting rotational distribution in the excited state is a mapping of the ground state rotational distribution and can be used to determine the gas temperature. The situation is however significantly more complicated when the excited states are produced by electron impact dissociation, photoexcitation, metastable excitation or chemical reactions in general. In this case, the nascent ro-vibrational distribution can deviate significantly from the equilibrium Boltzmann distribution [83]. In this case, collisional rotational energy transfer should redistribute the excited state rotational levels significantly faster than the radiative lifetime of the excited state otherwise the measured rotational spectrum will be impacted by the production process of the electronically excited state and not necessarily be a good representation of the translation or gas temperature. The phenomena of non-Boltzmann rotational distributions have been studied for many decades [84], [85], [86] and have been reviewed in detail specifically for low temperature plasmas in [83].

Bruggeman *et al*. [87], [88] illustrated that departures from equilibrium rotational distributions can be substantial, even in highly collisional discharges. The rotational distribution of OH(A) may deviate from Boltzmann equilibrium, manifesting an excited state rotational level distribution that can be fitted by multiple distinct temperature parameters. In atmospheric pressure water vapor, the collisional quenching time of OH(A) by H_2O is comparable to the time needed for rotational relaxation. As a result, the rotational population distribution of OH(A) falls short of reaching thermal equilibrium. Consequently, the distribution is strongly influenced by the formation process, often resulting in a non-Boltzmann distribution. Nonetheless, the rotational energy transfer rate is a function of the rotational level and thermalization of the rotational levels with lower rotational quantum number can be considerably faster than for higher rotational levels [89]. This might enable it to still determine the gas temperature from such spectra from the initial slope of the Boltzmann plot. An example is shown in **Fig. 10.** An alternative cause of a two-temperature distribution is a combination of two processes to produce OH(A): electron excitation of ground state OH(X) and dissociative electron excitation of H_2O [90], [91]. Interestingly, a ro-vibrational spectrum of OH(A-X) reported for microsecond pulsed streamer discharges can be fitted with a rotational temperature of 5000 K and a vibrational temperature of 800 K [11]. The significantly lower vibrational temperature compared to the rotational temperature is a nice example of the highly non-equilibrium plasma state for which we need to be exceedingly careful in interpreting not only rotational but also vibrational temperatures.

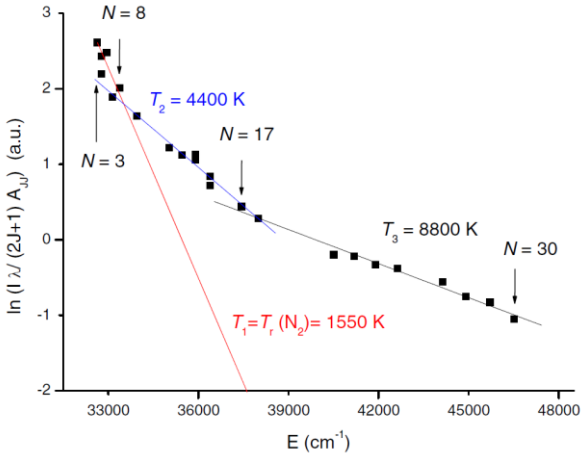

Figure 10: Boltzmann plot of the rotational distribution of OH(A) deduced from a spectrum of a plasma in a vapor bubble containing air impurities. The N_2(C) spectrum is produced by electron impact excitation and enables the estimation of the gas temperature equal to 1550 K. This gas temperature coincides with the initial slope of the OH (A) rotational distribution function. Reproduced with permission from [83].

Similarly, ro-vibrational spectra of other diatomic molecules like C_2, N_2 or CN for carbonaceous liquids and liquid nitrogen [92], [93], [94] must be analyzed with caution as well. Correlating rotational with gas temperatures is often impossible. This is especially true for discharge in liquids where species contributing to emissive systems exist in both liquid and gas phases. For example, Ingebrigtsen *et al*. [94] produced streamers in chlorinated alkane and alkene liquids by applying high-voltage pulses (-30 kV, 0.1/50µs) in a pin-to-plane configuration. Discharges are close to pLTE, but rotational and vibrational temperatures of the C_2 molecular probe are never in equilibrium, vibrational temperatures being maximum twice as large as the rotational. By calculating the net emission factor in the plasma, these authors could deduce atomic excitation temperatures close to 12,000 K. The rotational and vibrational temperatures deduced from the shape of the C_2 Swan bands were much lower: ~2,500 K and 4,000 K, respectively. This is an example of a study where the plasma has a strong dissociation degree in the core and likely very high temperatures (reflected by the atomic excitation temperatures) and C_2 molecules are produced by atomic C recombination in the plasma zone at lower temperatures surrounding the atomic plasma core (C_2 rotational temperatures might reflect conditions in this lower temperature plasma zone).

ii. Self-absorption in molecular spectra

Similar to atomic spectra, self-absorption is also possible for molecules. The analysis of self-absorption in molecules is less developed compared to their atomic counterpart although the effect has been used as a measurement approach to measure the OH ground state density from emission spectra in a diffuse homogeneous glow discharge in helium – water vapor [95]. In this case the parameters needed to fit the recorded emission spectrum not only include the rotational temperature of the excited state but also the rotational temperature of the ground state and the ground state density. It is obvious that for inhomogeneous discharges, it might become challenging to analyze the spectra as the spatial distribution of these 3 parameters needs to be considered and additional non-equilibrium effects as discussed above might also be present.

iii. Continuum molecular emission

Molecules are also able to produce continuum emission. Arguably the most well-known is the hydrogen and deuterium continuum UV emission [96]. Emission of broad molecular continua in the visible range is often observed in liquids consisting of long molecular chains such as alkanes, benzene,

cyclohexane, etc. In these molecular systems, since all excited states with energy higher than that of the weakest chemical bond can dissociate, there is the formation of fragments in the excited or ground state. The following references [94], [97], [98] report examples for discharges initiated in cyclohexane and n-pentane. By increasing the hydrostatic pressure, and then the density in the channel and the collision frequency, the vibrational energy of the molecules can relax before dissociation and the production of excited C_2 molecules decreases. This facilitates the detection of a molecular continuum that is approximately constant from 450 to 850 nm [98]. Rogza and Tabaka [99] attributed the emission between 380 and 600 nm for natural and synthetic esters, to dissociation and fragmentation of molecules. Gamaleev *et al.* [100] also observed, but in highly conductive seawater, that an increase in pressure causes a strong increase of the emission of a flat continuum in the visible range.

One difficulty is to avoid confusing molecular emission, when it is spread over the entire visible range, with continua emitted by particles or potentially other sources of continua (see below). For example, Lebedev *et al.* [101] explained that their attempts to measure the line emission from discharges in benzene were unsuccessful because the spectra were due to continuum emission from solid particles. These particles emit broadband continuum emission that can be processed as the emission from a Planck radiator.

iv. Case study: State-to-state modeling of OH luminescence spectra in combustion

Intrinsically the analysis of non-equilibrium ro-vibrational spectra to date in plasmas in liquids is partially empirical by fitting multiple temperatures to a non-Boltzmann distribution. As discussed above, ro-vibrational spectra might provide information about the formation process of the excited state and fitting that consider the formation process and the collisional environment would allow us to fit spectra purely based on physical principles. To our knowledge, such an approach has not been implemented for plasmas in and in contact with liquids. However, state-to-state modeling of chemiluminescent spectra has been reported in the combustion community [102]. An example is shown in **Fig. 11**.

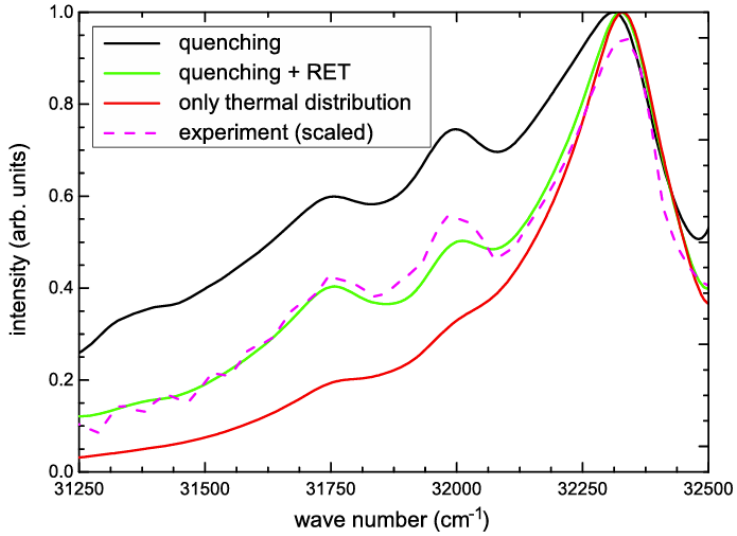

Figure 11: OH chemiluminescence spectrum from a flame (magenta dashed line) compared to simulated spectra obtained by the spectrum calculated considering detailed state-to-state collisional energy transfer processes and assuming a nascent A state rotational distribution with $T_{nascent}$ = 5000 K. Black: collisional quenching is considered. Green: Both Quenching and rotational energy transfer are considered. Red: simulated emission spectrum of a thermal rotational distribution with T_{gas} = 2200 K – reproduced with permission from [102].

The state-to state chemiluminescent spectra model is basically a modified laser induced fluorescence model (see further) in which the laser excitation typically of a single rotational is replaced by assuming

a nascent rotational distribution due to the formation process of the excited state (in the case of **Fig. 11** a Boltzmann distribution with a temperature parameter of 5000 K is considered), although in principle any nascent rotational distribution can be considered. The models incorporate collision transfer reactions including collisional quenching and rotational energy transfer and the radiative processes of the excited state. In principle, the model allows to obtain more information about the nascent rotational distribution and the dominant production processes of the excited state which could shed additional light on the complex plasma conditions in liquids.

c. Continuum radiation

The origin of continua in discharges in liquids can be multiple. Continuum emission can be generated by the heating of the medium, the electrodes and the formed particles, that behave as blackbody emitters. It can also be due to the dissociation of large molecules into fragments that radiate broad molecular emissions as already discussed above. In addition, free-free or free-bound emissions due to electron-neutral or electron-ion collisions also referred to as Bremsstrahlung can be an important emission source in plasmas although it depends strongly on the electron (and neutral) density of the discharge. Equations for these different phenomena giving the evolution of the emission intensity as a function of wavelength can be found in [19]. The measurement challenge related to continuum radiation for plasmas in and in contact with liquids is determining the origin of the continuum radiation. We focus in particular on the role of Planck`s emission vs Bremsstrahlung as a case study but first explore continuum emission through the perspective of the arc discharge community.

i. Continuum emission and arc discharge

The high electron density in arc discharges leads to significant continuum radiation that has been investigated in detail often through the use of the net emission coefficient approach [103]. For example, Adineh [104] calculated the radiative heat loss for electric discharge machining based on arc plasmas in liquid nitrogen using the net emission coefficient method. The results from pressures equal to 0.1 and 1 MPa and working temperatures between 5500 and 10 000 K indicate that the free-bound mechanism should be the dominant contributing emission mechanism in the continuum radiation compared to the others.

In the case of free-bound recombination radiation, since the upper level is continuous, the radiation is continuous. However, there are some structures due to the discrete nature of the lower energy levels, called absorption edges. The spectra are then characterized by their specific sawtooth shape. Descoeudres *et al*. [61] explain that the extreme densities found in the early stages of discharges produced in EDM processes destroy the upper energy levels of the atoms, making the free bound radiation more important than the line radiation. However, there is no clear evidence that such continua have unambiguous absorption edges.

The analysis of any continuum observed in spectra first requires the recorded emission to be corrected for the optical response of the spectrometer. Once this is done, the shape of the profile can be compared with the spectral radiance (in W m^{-2} sr^{-1} Hz^{-1}) given by the Planck distribution law for a black body. In principle, many discharges in liquids take place at high temperature (T_g ~ T_e ~ 1 eV) and the medium behaves as a blackbody, emitting a continuum of light (**Fig. 12a**), which is actually composed of a large set of convoluted individual lines [19], [57].

Finally, Descoeudres *et al*. [62] sum up the ambiguity in the analysis of continua quite well: "*It is likely that this continuum is due to free-bound transitions (recombination processes). Free-free radiation is another plausible source. Since molecules generally emit a broadband spectrum, molecules or fragments of molecules from the dielectric are certainly involved in the continuum*". The many

possibilities associated with the emission of continua require the provision of independently assessed reliable data to discriminate unambiguously between the various contributions. In recent years, a more detailed analysis of continuum radiation of pulsed discharges has been reported which is addressed in the next paragraph.

ii. Case study: Planck's emission *vs* Bremsstrahlung

There remains continued debate about the origin of continuum radiation in pulsed discharges in liquid water. Bílek *et al*. [105] observe continuum emission at very short times, between 0 and 3 ns, during the initial phases of nanosecond pulsed discharge in liquid water. The applied voltage reaches 100 kV after 7 ns. They attribute this to the electron-neutral Bremsstrahlung process (**Fig. 12b**). In this case, the maximum energy of the photons is the initial kinetic energy K_0 of the electrons. The energy spectrum therefore stops at this value. If we plot the spectrum as a function of the wavelength, it starts at $\lambda_0 = \frac{hc}{K_0}$, which is indeed what is observed experimentally. The shape of the spectra depends on the choice of the electron energy distribution function, and an accurate model is obtained by introducing a Gaussian function. This assumption assumes the emission of a kind of electron beam at the peak energy of the functional. With this new parameter, electron temperatures around 2 eV are found. It remains difficult to understand why the electron energy distribution function should adopt a Gaussian functional dependence [105] if the discharge is supposed to be close to the LTE (which is typically reached on timescales of tens of picoseconds [106]).

In their experiment, von Keudell *et al.* [59] measured an electrode voltage close to 50 kV after 5 ns, but attributed the continuum emission they observe to blackbody radiation with two components, one with temperatures of 6000-7000 K at the very beginning of the discharge and one with temperatures of around 20,000 K appearing after 8 nanoseconds (**Fig. 12c**). The first values are close to the boiling temperature of tungsten, the metal of which the anode is made. The authors suggest that this component of the emitted blackbody radiation probably originates from the hot tungsten electrode with an additional contribution from hot spots [59].

Grosse *et al.* speculate that sharp protrusions on the tungsten tip electrode could play a role in the life of the electrode compared to, for example, Ir/Pt alloys which are smoother. However, this difference is seen over a time scale of one hour and should only give similar results after several discharges if two different tungsten wires are used. Furthermore, OES spectra do not show any W lines, from 0 to 35 ns in one case and from 0 to 435 ns in the other case. Hamdan *et al*. [107] showed that metallic lines appear after ~100 ns (depending on the melting point of the chosen metal), which is the time required to heat metals close to the temperature needed for evaporation to occur. The lack of metal lines might suggest a lack of erosion of the anode at the very beginning of the discharge. The time required to heat a solid material is typically hundreds of nanoseconds if not milliseconds, for a refractory metal [108]. It is hard to imagine that a tungsten electrode could be hot after only two nanoseconds. Furthermore hot tungsten is oxidized if its temperature is elevated at 7000 K in water (and unlike to liquid nitrogen [57], [109]). Hence, one would expect that during the first discharge the surface is transformed into WO_3, whose melting point is much lower than that of the refractory metal (1,746 K *vs* 3695 K).

The apparent contradiction between these two very similar experiments of the German and Czech research groups is striking. Even the gap distances (10 vs 5 mm) and the radii of curvature of the electrodes (25 *vs* 50 µm) are close. Furthermore, Grosse *et al*. [59] postulate that the onset of the discharge luminosity coincides with the onset of the HV pulse and that the dominant source of the observed continuum is a hot tungsten surface. Šimek *et al*. [110] showed that the onset of the discharge luminosity with a delay of several nanoseconds with respect to the HV pulse occurs and that all emissions originate from the luminous filament developing in the bulk liquid.

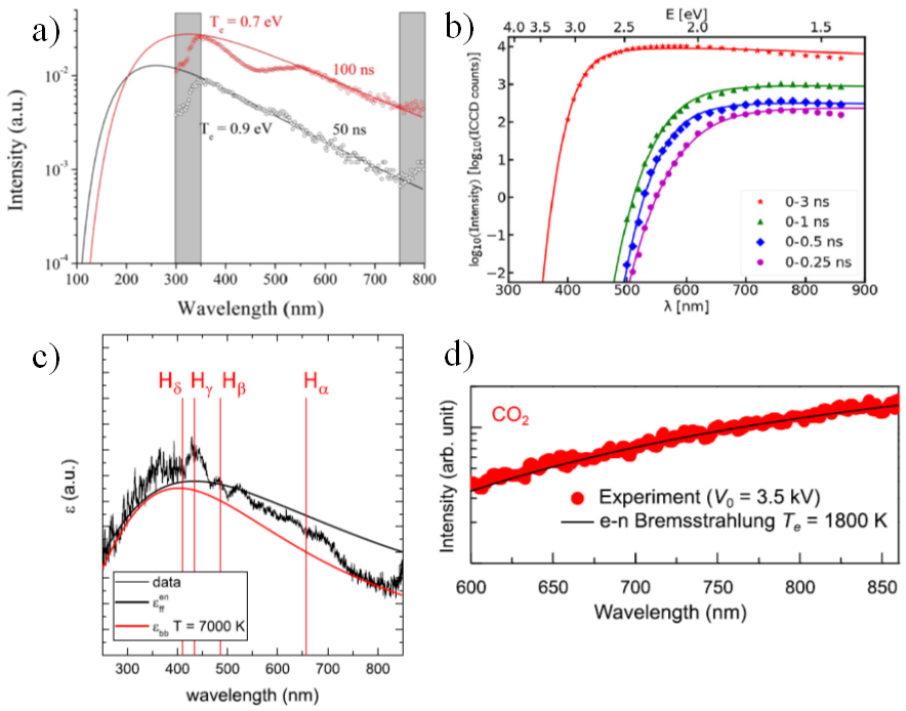

Figure 12: a) Blackbody continua observed during discharges in liquid nitrogen [57]. b) Continua observed by Bílek *et al*. and modelled with bremsstrahlung (free-free) emission [105]. c) von Keudell *et al.* [59]. d) Kawamura *et al*. [111].

The difference in the origin between the continua observed by the two groups of authors might be due to the intensities of the currents flowing through the electrodes. In the German group, the current is around 10 A with a deposited energy of 0.3 mJ/pulse vs 0.3 kA for the Czech group with a deposited energy of 0.3 J/pulse. Then, results might not be inconsistent as it might seem at first sight. The shape of the spectra (**Fig. 12**) suggests different mechanisms might be at stake. Continua might be governed by Planck's law at low current and by free-free (electron-neutral) bremsstrahlung at high current.

Simeni *et al.* [112] investigated this conundrum in more detail by performing absolute emission intensity measurements on a nanosecond pulsed liquid phase discharge with voltage amplitude more than 50 kV very similar to the study of von Keudel and Bilek although with a less sharp tungsten electrode tip. They showed that the shape of the continuum spectrum looks very similar to the spectrum of a blackbody at temperatures of ~ 1 eV. However, the absolute black body emissivity is many orders of magnitude higher than the experimentally measured absolute radiation. They concluded that black body radiation cannot be responsible for the measured continuum emission and ascribed the emission to Bremsstrahlung. Furthermore, they measured both the initial pulse which emitted only continuum radiation and subsequent discharges due to high voltage reflections that emitted both continuum radiation and atomic lines. Interestingly, the continuum radiation for the case in the presence of atomic lines has a lower plasma density and is suggested to contain both contributions from Bremsstrahlung and UV hydrogen continuum suggesting the discharge is generated in a vapor/gas phase.

Song *et al*. [109] also studied nanosecond pulsed discharges in water using a similar experimental setup. The applied voltage was slightly lower (20 kV) than Bilek *et al*. [105] for about 10 ns. Their pin electrode was made of steel. These authors observed continuum emission in the UV, which they assumed to be electron-neutral bremsstrahlung (current and energy per pulse are not provided). They did not observe any blackbody continuum or atomic lines. The possibility of a molecular emission in the UV is also high.

Marinov *et al*. [113], also with a similar experimental setup, observed with an applied voltage of 6 to 15 kV an intense continuum between 300 and 800 nm, "only" recorded after 40 ns and still observed after 260 ns, which could be fitted with the blackbody emission curve at 7000 K. Since nickel lines are found in the spectra, it is likely that nanoparticle emission is responsible for this continuum. Interestingly, as in the PEO process, these authors suggest that the H_α line consists of two contributions, emitted from a hot core and a colder peripheral region. Again, the H_α line could have been fitted with only one contribution by using Griem's profiles.

Miron *et al*. [114] also highlighted the role of nanoparticles in the emission of blackbody radiation. Each nanoparticle acts as a hotspot emitting from the electrode. The authors observe broad emission continuum spectra in the range of 350–940 nm with tantalum electrodes, but not with tungsten electrodes. They explain this behavior not only by the different melting points of the tungsten (3,695 K) and tantalum (3,290 K) electrodes, since they determine a blackbody temperature of about 4,500 K, but also by the injected power, which was 10-20% higher for the Ta electrodes than for the W electrodes. They suggest that the higher energy input per pulse for the Ta electrodes could be the result of the oxide layer formed on the electrode surface, the oxidation process being higher for the Ta electrodes than for the W electrodes.

In the experiments of Lebedev *et al*. [115], based on microwave discharge (2.45GHz, 200–500W) in liquid alkanes, the broadband continuum is observed only in time-averaged discharge spectra, but not present in one-shot recordings over 1 ms. They attribute this behavior to solid carbonaceous particles whose concentration is so low that averaging is required to see their emission.

Kawamura *et al*. [111] measured continuum optical emission spectra in a field-emitting surface dielectric barrier discharge, using 10 kHz ac excitation, studied in liquid CO_2 at pressures from 6.8 to 7.6 MPa and temperatures from 290.9 to 291.4 K. They attribute the discharge emission to electron-neutral bremsstrahlung, the recorded spectrum then being easy to fit (**Fig. 12d**).

In conclusion, the complexity and highly transient nature of the discharge makes it challenging to explain in detail continuum emission spectra to date. Nonetheless, more detailed explanations have been provided in recent years although discrepancies in explanations need to be addressed. Using absolute emission intensities would provide more quantitative information to assess the validity of different fitting or model approaches which has currently not been a focus of the field.

4. Early stage and ultrafast processes

The occurrence of discharges in liquids (without the presence of pre-existing bubbles) inevitably involves ionization processes and a phase transition at some point during or after the discharge generation from the initial liquid state to the final gaseous state of the formed bubble. In some cases, direct ionization in the liquid phase is proposed to occur due to direct electron impact "without undergoing a phase transition" [116], [117]. Numerous mechanisms have been explored, which are not only dependent on the properties of the liquid but also on its polarity. These include electronic avalanches, field-assisted ionization, field-assisted dissociation (Onsager), photoionization, among others, all of which have been extensively discussed in studies on pulsed discharges [118]. A body of work [119], [120], [121], [122] has shown in several atomic and molecular liquids that the "dense gas approximation" is not valid for liquids. In many cases, the electric fields are highly non-uniform, and the electric fields needed for direct ionization in a dense medium with short voltage pulses are huge, and consequently induce electrostriction within the liquid. This mechanism efficiently reduces the liquid density and occurs over durations that scale with $2R_c/c$, equating to picoseconds for curvature

radii R_c of 100 µm (**Fig. 13**). This puts stringent requirements on the temporal resolution required to study such phenomena.

Considering the density of water (around 1000 times higher than that of vapor), along with the temperature increase, and accounting for the dissociation of water (increasing the density at most by a factor of three), as well as the ignition initiating in a region rarified by the constriction mechanism (reduced by a factor around 0.3, as depicted in **Fig. 13**) [123], the pressure can reach a maximum of approximately 10,000 times atmospheric pressure. In practical terms, for an electric field strength of approximately 10^9 V m^{-1} [124], the initial pressure should be closer to hundreds of bars. It is noteworthy that beyond a temperature of 1000 K, water at equilibrium exists either as vapor, which can be highly pressurized, or as supercritical fluid below 100 GPa [125]. In addition, the discharge channel formed in the liquid can extend axially at supersonic velocities, typically reaching hundreds of km s^{-1} [126], and up to 5000 km s^{-1} at inception [116] and diagnostics needs to be able to capture these phenomena with sufficient temporal and spatial resolution. The above summary stresses the need for accurate measurements of the electric field, phase change and ultrafast ionization processes for such experiments in addition to the need for high spatial resolution. We discuss these aspects below in more detail.

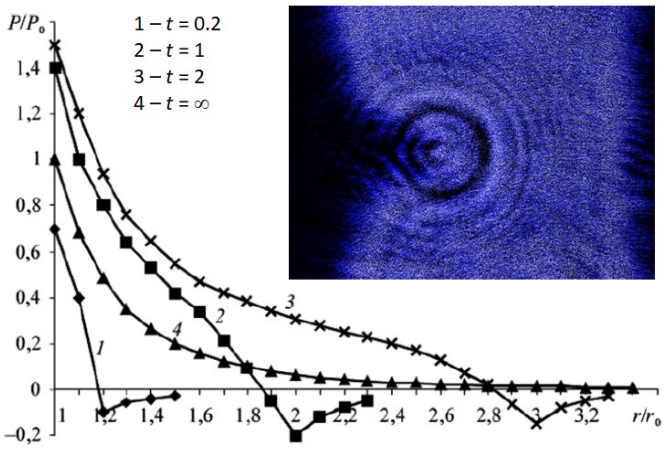

Figure 13: Dependence of the normalized electrostriction pressure on the radius at the indicated time moments from the impulse voltage application to the spherical electrode. The minimum of the rarefaction wave is found at t = 2 in the example. Reproduced with permission from [123]. Insert: The electrostriction rarefaction wave without breakdown in liquid water. The applied voltage is 9 kV with a width of 20 ns. The image was collected 200 ns after the HV pulse. Reproduced with permission from [117].

a. Initial phase change

Phase change in liquids is relatively straightforward to measure using shadowgraphy or interferometric approaches [11], [117]. Nonetheless, measurements are limited by the optical diffraction limit and the time resolution is often significantly impacted by jitter in the discharge generation. An example of the visualization of electrostriction effects is shown in **Fig. 13**. Recently the group of Staack has extended this with ultrafast X-ray measurements [127]. This technique provides interesting opportunities as shown for the measurement of cavitation bubbles and shockwaves induced by plasmas generated in liquid at plasma initiation timescales. It was furthermore shown that the technique can resolve narrow low-density plasma channels at these timescales, conditions for which the strong emission in the channels might prevent accurate measurements of the refractive index change of the medium.

Nonetheless, this approach utilized the Argonne National Laboratory's Advanced Photon Source a capability much beyond the usual tabletop approaches leveraged in our field.

b. Electric field measurements

A range of different optical diagnostics have been developed for electric field measurements with a strong focus on gas phase plasmas. This includes Stark polarization emission spectroscopy leveraging the shifting and splitting of light atoms such as H and He [128] or line or band intensity measurements [129] which are unfortunately not directly applicable to liquid phase plasmas due to the significant collisional broadening and complex sources of emissions.

Laser based techniques have been developed for low pressure plasmas including fluorescence dip spectroscopy [130]. Electric field measurements that are compatible with a high collisional environment include electric field-induced coherent Raman scattering (CRS). Nonetheless, the technique is limited to Raman active gases and has been mainly used in N_2 and H_2 plasmas [131]. More recently, electric field-induced second harmonic (EFISH) generation has been shown to be a powerful and versatile technique for electric field measurements in plasmas [132]. The only requirement is that the gas has a reasonable polarizability and so can be used in most high-pressure plasmas. The time resolution of the measurement is limited only by the laser pulse duration. Unlike CRS, EFISH is species-independent [132]. While CRS has been used to measure the electric field in plasmas with liquid electrodes [133], to our knowledge it has not been attempted to study liquid phase plasmas.

Mach–Zehnder interferometric measurements have been reported to measure the electric field in liquid water near the metal electrode near breakdown conditions [133]. The approach analyzed the phase shift of light in the liquid induced by the electrical field stress by leveraging the Kerr effect. Furthermore, it has also been used to measure the field enhancement near a propagating streamer head in liquid [134]. It would be interesting to explore how developments in atmospheric pressure plasmas in the last decade could be further leveraged to enhance the temporal resolution of electric field measurements in liquids.

c. Case study: Ultrafast liquid phase (ionization) processes

Ultrafast processes, such as the solvation time of solvated electrons, which is reported to be in the 10s of ps have been extensively studied using pico- or even femtosecond lasers [135]. While techniques to interrogate electron dynamics on these timescales are available, they are exceedingly challenging to couple with electrically produced discharge plasmas due to their inherent jitter which is typically on the nanosecond timescale. The study we want to highlight uses a femtosecond laser to generate plasma in liquid water and allows well-aligned pump-probe measurements with picosecond time resolution. Sakakibara *et al*. [136] studied the generation and decay of solvated electrons by a femtosecond laser pulse by interferometry. The key result from their work is shown in **Fig. 14**. They observed additional solvated electron generation after the pulse. This is attributed to the abundant free electrons in the laser-produced plasmas. These visualized processes are exactly the processes and timescales that are of interest in electrically produced plasmas in liquids. Further studies might be very useful to gain more insight into ionization processes in liquids particularly if they could be conducted in the presence of electric fields.

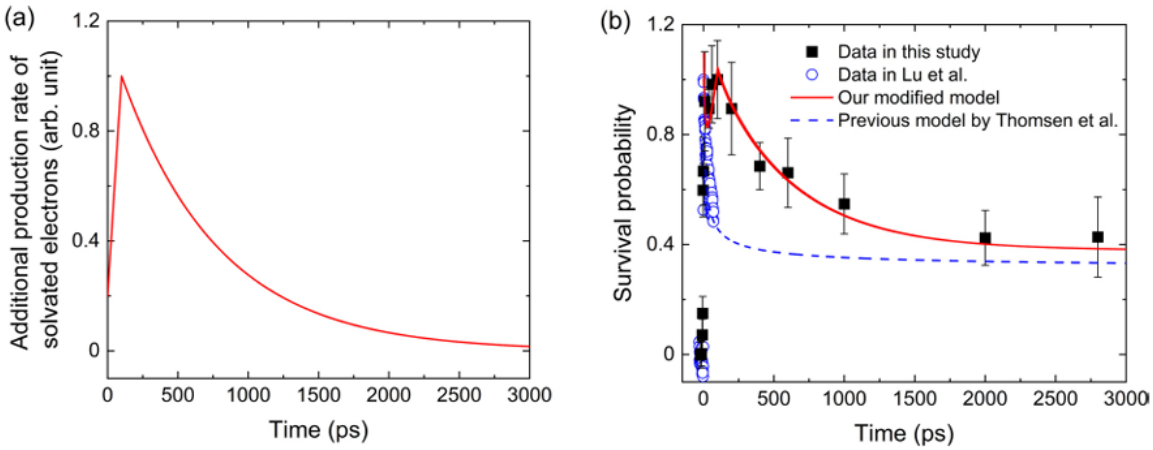

Figure 14. Solvated electron generation and decay induced by a plasma in the liquid phase generated with a femtosecond laser. (a) Deduced production rate of solvated electrons on < 1 ns. (b) Comparison of model and experiment of the decay kinetics of solvated electrons. Reproduced with permission from [136].

5. Plasma-liquid interactions

In the case of plasmas in liquids the most used diagnostic approach is OES, the focus of section 3. OES is indeed a powerful tool to study plasma physics, and the key goal is determining the main plasma characteristics such as electron density and gas temperature. Nonetheless, a major focus of research involving plasmas in and in contact with liquids leverages plasma-induced liquid phase chemistry for a variety of applications. A quantitative understanding of these processes involves the measurements of reactive species composition and density in both the gas phase plasma and the liquid phase. Unfortunately, detailed measurement of the gas and liquid phase species at the plasma-liquid interface remains challenging due to the huge species gradients both in the liquid and gas phase. These near spatial gradients are strongly impacted by the bi-directional interaction of the plasma with the liquid. In addition to a flux of reactive species from the plasma to the liquid, the plasma will induce evaporation and transfer of species from the liquid to the gas phase as well which can directly impact the local plasma properties near the plasma-liquid interface. We present the challenges, recent advancements and opportunities for species density and concentration measurements below.

a. Species density measurements in the gas phase

A broad range of diagnostics techniques have been implemented to characterize the species densities in gas-phase plasmas in the last several decades. These techniques have been leveraged from different communities including the combustion and gas sensing communities. OES, while extensively used for reactive species measurements in low pressure plasmas, for example through actinometry [137], is not always ideally suited to probe reactive species in most situations for highly collisional near ambient pressure plasmas generated in a complex gas mixture as relevant for plasma-liquid interactions.

i. Commonly used gas phase diagnostics

Absorption spectroscopy is one of the most direct approaches to measuring species densities [138]. A broad range of different absorption spectroscopy approaches have been developed and implemented including broadband, tunable diode laser, cavity enhanced and cavity-ringdown absorption spectroscopy [139], [140], [141], [142]. While absorption spectroscopy requires minimum assumptions, the technique is inherently a line-integrated measurement which becomes more challenging for non-homogeneous plasmas. Nonetheless, successful examples of using for example broadband absorption to determine the OH density distribution in a dc glow discharge in contact with liquid have been

reported [143]. In this case, it was assumed that the plasma was cylindrical symmetrical to allow for species densities profile measurements using Abel inversion.

Laser-based diagnostics are extensively used to measure species densities in inhomogeneous and transient plasmas. Nanosecond and more recently picosecond and femtosecond lasers enabled the temporal and spatial variation of both short and long-lived species in a plasma [144], [145]. The most common laser diagnostics that have been leveraged by the community to study plasma-liquid interactions include laser induced fluorescence (LIF) for the measurement of diatomic radicals like OH, NO and gas temperatures [7], two-photon absorption LIF (TALIF) for measuring atomic radicals like O, H and N [146], and Thomson scattering for measuring electron densities and temperatures [147].

Most laser diagnostic studies have focused on the measurements of the bulk concentration of species of interest. Nonetheless, at typical near ambient pressure conditions, sheaths and boundary layers have length scales of 100 μm or less [148] and this length scale needs in principle to be resolved if such techniques are used to determine the flux of reactive species into the liquid phase. The usual dynamic nature of the liquid interface with likely displacements on a similar or even larger length scale than the desired spatial resolution is a major impediment for such measurements. In addition to plasma stabilization, a major effort is to establish plasma systems with a highly stabilized and well-defined and controllable plasma-liquid interface (see section 2). Mass spectrometry, and in particular, molecular beam mass spectrometry (MBMS) has been a tool that has been extensively used for measuring plasma-produced species fluxes at plasma-solid interfaces. Unfortunately, the intrusive sampling of MBMS is incompatible with a plasma-liquid interface and optical diagnostics remains the preferred approach to characterize near interfacial plasma-liquid interactions.

The most common study in this context is likely OH LIF during the interactions of plasmas with aqueous solutions. In a highly collisional environment, a LIF model describing collisional energy transfer processes in addition to laser excitation and radiative decay (see **Fig. 15a**) is required to obtain the OH density [149]. The derived density can be very sensitive to the local gas composition which is inherently unknown near the plasma-liquid interface due to the evaporation. This is particularly the case for water vapor which is a highly effective quencher of laser excited OH(A). The measurement of the lifetime of OH(A) can have challenges particularly for nanosecond pulsed lasers if the water vapor density is too large. On the other hand, in some cases, the water concentration can be determined from the OH(A) lifetime near the plasma-liquid interface [17], [150]. The most common approach to absolutely calibrate the OH-LIF signal is with Rayleigh scattering on a known gas at a known pressure and temperature. Several research groups have reported spatially and temporally resolved distributions of plasma produced OH radicals as well as water vapor densities near the plasma-liquid interface indicating both significant evaporation and increased OH generation compared to the bulk plasma [17], [150], [151]. Nonetheless, the spatial resolution of the LIF measurement near the plasma-liquid interface was not always sufficient to deduce accurate species fluxes towards the liquid. These measurements are also dependent on the shape of the interface between the two phases and on the hydrodynamic movements of both fluids over longer time scales.

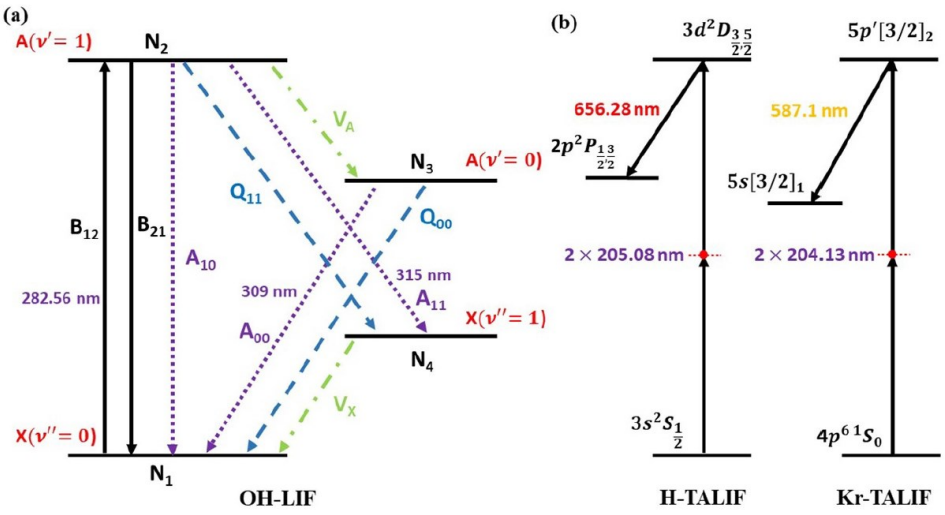

Figure 15. (a) Schematic of the transitions involved for OH LIF considering 4 vibrational levels (4-level LIF model) with the assumption that the rotational levels obey a Boltzmann distribution. A_{ij} are Einstein emission coefficients, B_{ij} Einstein absorption coefficients, Q_{ij} collisional quenching rates, V_i vibrational energy transfer rates and N_j the density of indicated vibrational level *j*. (b) Energy diagram including the excitation and emission processes for H-TALIF and Kr-TALIF (typically used for absolutely calibrating H-TALIF measurements). Reproduced with permission from [152].

The measurement of reactive species densities such as OH in discharges in liquids have not been achieved to date. The inherent stochastic nature of the liquid discharges combined with the fast and large variations in the gas composition and pressure makes it exceedingly challenging. Nonetheless, OH-LIF has been recently applied to a discharge in a vapor bubble [14]. This was enabled by a repetitive controlled generation of a vapor bubble in a Hele-Shaw cell using a voltage pulse of about 1 ms which allowed the accumulation of the LIF signal over multiple reproducible discharge events. Interestingly, the high-pressure water vapor in the bubble does not allow one to assume that the rotational levels of the laser pumped vibrational level are obeying a Boltzmann distribution, a requirement to use a 4-level LIF model describing the energy levels in **Fig. 15a**. In this case the analysis of the LIF signal was performed with a state-to-state resolved LIF model considering 160 rotational levels for each vibrational level.

The locally increased water vapor concentration near the plasma-liquid interface due to evaporation can have a significant impact on the local plasma properties. Indeed, Yue and Bruggeman [153] reported Thomson scattering measurements of the electron density and temperature near a NaCl solution anode in a helium plasma. They observed a decrease in electron density and significant increase in the electron temperature when approaching the solution anode due to the enhanced electron losses with increasing water concentration in the helium plasma. While the impact of water evaporation on plasma properties has received considerable attention, also in modeling studies [154], [155], solutes such as dissolved salts from solutions can also transfer into the plasma phase and have a significant impact on the plasma properties. This is particularly the case when metallic cations from salts can form atoms in the plasma which can have much lower ionization energies compared to water vapor and other commonly used gases such as argon and helium. In spite of the fact that the transfer of solutes from the liquid phase to the gas phase has been used to analyze the concentration of metals in solutions in the field of analytical chemistry for more than two decades [156], [157], the underpinning mechanism of the solute transfer remains unclear. Only recently, the first quantitative study of solute transfer in a glow discharge with liquid cathode has been reported [158]. This study is an example of the use of planar femtosecond TaLIF to measure the spatial and temporal buildup of sodium atoms in the plasma near the plasma-liquid interface. While OES can show the presence of sodium in the plasma, the absolute densities obtained by TaLIF in this study uniquely allowed the

authors to analyze in more detail the mechanism underpinning the transfer of solutes from the liquid to the plasma phase.

ii. Case study: Absolute gas phase species flux measurements

Apart from electron fluxes in DC-driven discharges for which the electron flux can be directly deduced from an electrical current measurement, quantifying the flux of plasma-produced reactive species to a liquid interface, while critical, remains largely unexplored. Yue *et al.* [17] recently reported the measured flux of OH radicals obtained by high resolution planar LIF by a helium glow discharge plasma with a liquid anode. The OH density distribution near the plasma liquid interface is shown in **Fig. 16.** The required spatial resolution of 30 µm to be able to obtain the gradient in OH density near the plasma-liquid interface was achieved by using a stabilized convex liquid interface as shown in **Fig. 2**. The OH and electron fluxes determined for a pulsed glow discharge with pulse width of 9 µs is shown in **Fig. 16**. The authors used these measurement outcomes together with the determined electron flux as the input for a liquid phase transport and chemical kinetics model that was able to successfully explain ferricyanide reduction. As plasma-induced liquid phase chemistry is enabled by gas phase fluxes of reactive species to the liquid phase and current models do not always have a detailed description of plasma-induced evaporation, more detailed measurements of reactive species fluxes to the liquid phase directly correlated with liquid phase plasma-induced chemistry are needed to gain a more refined understanding of plasma-induced liquid phase chemistry.

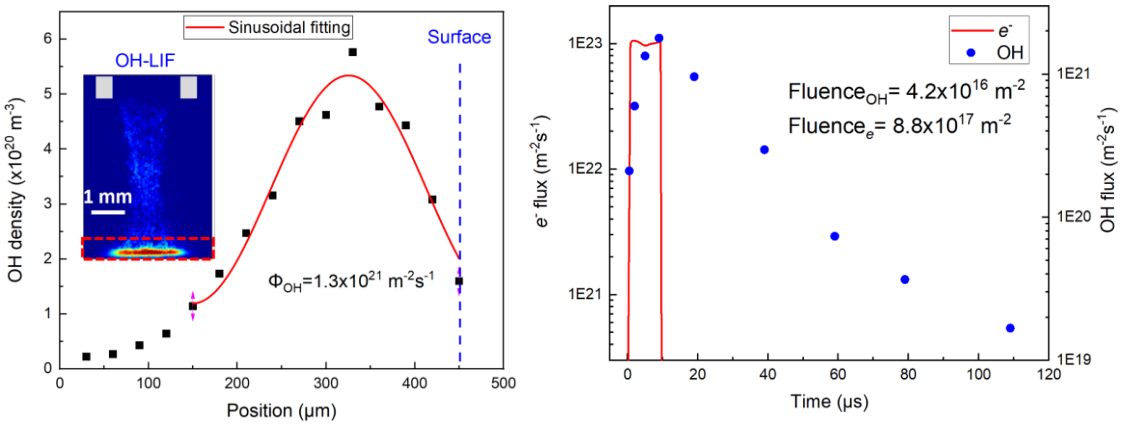

Figure 16. (left) OH density distribution near the plasma-liquid interface (position at ~ 450 µm). (right) The electron and OH flux to the liquid surface as a function of time for a pulsed atmospheric pressure glow discharge with a pulsed duration of 9 µs. The OH flux was determined from the axial gradient of the OH density near the liquid surface. The electron flux is determined from the conduction current measurements. Reproduced with permission from Yuanfu Yue and from [17].

b. Selective reactive species density measurements in the bulk liquid phase

The field of analytical chemistry has developed many approaches to analyze the composition of solutions. Nonetheless the unique aspect of plasma-treated solutions is that they consist of stable and non-stable intermediates and reactions products which often remain reactive on much longer timescales than the plasma treatment time and the selectivity of the analytical approach becomes critical.

i. Commonly used liquid phase diagnostics

Selective analytical approaches enabling the identification of plasma-produced liquid phase species include ICP-OES, liquid and ion chromatography, electrochemical sensors and mass spectrometry [159], [160], [161], [162]. In view of possible reactions between the solution constituents, immediate fixation of any liquid samples is often a key step when measuring plasma-produced species (either by radical quenchers or suitable buffers) [163].

Similarly to gas phase diagnostics, many optical measurements are available for the analysis of solutions. For example, absorption spectroscopy has been used to determine the amount of NO_2^-, OCl^-, NO_3^-, dissolved oxygen and H_2O_2 in plasma treated solutions [164], [165]. This has been recently extended to the analyses of the conversion of larger hydrocarbon molecules for solution plasmas [166]. Nonetheless, most solutes have relatively broadband absorption profiles in the UV and visible spectrum that can significantly overlap and are often challenging to interpret. IR measurements are more challenging particularly for water which is a strong absorber for IR radiation. Colorimetric assays which utilize spectrophotometric approaches for quantification of species densities are often used [167]. In this case, the specific colorimetric reagent that is added to the solution reacts with the species of interest forming a color complex. It is assumed that the resulting absorbance by the color complex relates quantitatively to the number of species of interest present in the solution. A common colorimetric approach used in the field of plasma-liquid interactions is the measurement of H_2O_2 by the addition of titanium sulfate to the solution which yields a yellow titanyl sulfate complex upon reaction with H_2O_2 [167]. It is however exceedingly important to assess the selectivity of the reagent (as the detection relies on a chemical reaction) in view of the often many different reactive species present in the plasma-treated solution. Furthermore, fluorescent probes can also be used to detect plasma-produced species [168]. Fluorescent probes are typically more sensitive than colorimetric approaches but have similar selectivity issues. One way to assess selectivity of probes is to add scavengers and assess the impact of scavenging targeted species on the colorimetric or fluorescent signal.

Several of the available analytical techniques described above include sampling and are most often used to detect long-lived species. Nonetheless there remains a significant interest in the detection of plasma-produced short-lived reactive species and radicals in solutions such as NO, OH, O, O_2^- and O_3. However, reactive species and in particular radicals are difficult to measure due to their short lifetimes. Radicals with their unpaired electrons are paramagnetic. Electron paramagnetic resonance (EPR) spectroscopy leverages this property to quantify radicals at least for bulk solution measurements [169]. Unfortunately, in aqueous solutions the direct observation of the radicals is not possible due to their exceedingly short lifetime (and hence very small abundance or concentrations) under typical reaction conditions. Nonetheless, EPR measurements can be enhanced by using the so-called spin trapping technique [162]. This approach involves the addition of a spin trap compound and upon reaction of the radical with this compound a radical-spin-trap-adduct is formed with an increased lifetime and specific fingerprint signatures that allows for a detailed quantification with EPR. 5,5-dimethy-1-pyrroline-N-oxide (DMPO) is likely the most common spin trap used [170]. Unfortunately, the spin-trap approach increases the number of potential challenges considerably. In addition to selectivity that remains a possible issue, spin adduct stability, and their finite lifetime further complicate the interpretation of the measurements.

Colorimetric and fluorescent approaches can also be leveraged to detect short-lived species. Similar to the spin-trapping approach, the radical is measured indirectly through longer-lived species and hence such measurements have similar limitations as mentioned above. It is important to note that adding chemicals to detect species might also directly interfere with the solution being characterized. In addition, the obtained reaction product concentration can have a very complex relationship with the actual short-lived species densities. This is particularly the case for non-homogeneous reaction conditions, as present in many plasma-liquid interaction studies. Such conditions require careful analysis potentially including a detailed model. We come back to this in the case study below.

While in radiolysis, radicals have often been measured by absorption spectroscopy [171], this is much more challenging for plasma-liquid interactions because significant radical densities are only found near the plasma-liquid interface due to their finite lifetime and penetration depth while radical densities in the bulk liquid are expected to be well below the detection limit. *In situ* localized and fast measurements would be ideal to measure radicals and would allow us to measure near interfacial

concentrations which we discuss in detail after describing an interesting application of bulk liquid phase species concentration measurements in the following case study.

ii. Case study: Absolute species flux measurements through liquid phase analysis

While radical measurements in the (bulk) liquid remain challenging, interestingly bulk species concentrations measurements of long-lived reaction products of radicals can be used to determine the dominant radical flux to the liquid interface if one assumes a steady-state flux. An excellent example of this approach is reported by Jirasek and Lukes [172]. They used a colorimetric approach to measure the formation of OCl^- which was previously shown to be produced dominantly for O_2 containing plasmas through O radical reactions in saline solutions near the plasma-liquid interface [173]. The authors found that at high NaCl concentrations, the production of the colorimetric compound (and OCl^-) saturates **(Fig. 17**). This suggests that the production of OCl^- becomes independent of the transport of Cl^- to the plasma-liquid interface and is limited by the flux of O radicals from the plasma into the solution. When the amount of reaction products becomes independent of the initial concentration of the reactant, one can determine the amount of O radicals that were injected into the liquid phase. The determined O flux deduced from the liquid phase measurements shows excellent agreement with independent gas phase measurements of the O radical density flux (**Fig. 17**). If the radical would react with water or other compounds in the solution, corrections for such reactions might need to be made before an accurate flux can be deduced from bulk conversion measurements. This example shows that selected bulk concentration measurements of reaction products can be a very powerful approach to measure the total amount of plasma-produced radical species injected in a solution. While the approach does not require advanced laser diagnostics and can be achieved in many relevant cases, it is surprising that it is not more often used to enable the quantitative analysis of plasma-liquid interactions.

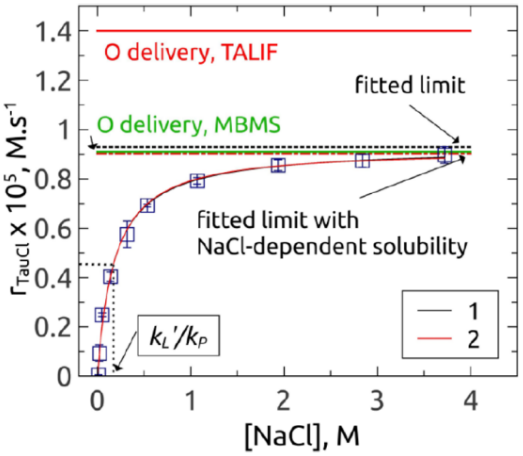

Figure 17. Production rate of TauCl (colorimetric agent used to detect the amount of OCl^- formed in solution), and plasma-produced O atom delivery estimated by molecular beam mass spectrometry (MBMS, green line) or TALIF (red line) as a function of the initial NaCl solution concentration. Reproduced with permission from [174].

The analysis of the formation of a reaction product in this case study can also be applied to colorimetric or spin-trapping approaches more generally. One can find many studies that report unrealistically large "average bulk radical densities" in excess of 1 µM in solutions. In some cases, reports go as far as making no distinction between spin-trap adduct concentrations and radical densities. We would like to offer the following thoughts. If indeed radical-induced reactions are dominantly occurring near the plasma-liquid interface, an averaged radical density is not a very useful physical quantity. Furthermore, the number of stable reaction products might be a better representation of the radical flux into the solution (as in the example of **Fig. 17**) than a "radical density" as the product concentration often increases with increasing treatment time (radical densities are typically in first approximation in quasi-steady state during a typical treatment time of seconds to minutes because of their short lifetime). In

addition, the result will be dependent on the concentration of the colorimetric or spin-trapping agent. Indeed, for low concentrations, the conversion rate will be transport limited (as in **Fig. 17**) and the amount of product is not even a good representation of the number of injected radicals into the solution.

We provide a canonical worst-case scenario for the above challenge: a micro-meter sized droplet falling through a homogeneous plasma while being subjected to a continuous OH flux identical to the conditions described in [16]. This paper has a transport model of formate conversion induced by OH radicals that can reproduce the experimentally obtained conversion. We deduce from the model the numbers in the table below for a condition that led to 50% formate conversion. In this case the conversion occurs at the plasma-liquid interface due to high concentration of OH radicals which penetrate less than 2 µm into the droplet. The bulk OH concentration remains according to the model well below the nM level as OH radicals rapidly react with the formate present. Interestingly, the flux of OH radicals into the droplet is about 17 times larger than the converted formate as shown in **Table 2**. This is because the formate is significantly depleted near the plasma-droplet interface and the transport of formate from the bulk of the droplet to the plasma-droplet interface is the rate limiting step for the conversion. Note that the amount of converted formate molecules (which could be seen equivalent to the number of reaction products formed as would be the case for a spin-trapping agent for example) is significantly larger than any OH radical density found in the droplet and is in this case not even representative for the OH flux into the droplet. Nonetheless if a sufficiently large formate concentration would have been used, the OH flux could be obtained similarly as in **Fig. 17**.

Table 2. Effective formate ($HCOO^-$) concentrations obtained from the experiment and the treatment of a 36 µm droplet for 10 ms in a He-H_2O glow discharge with an OH density of 3×10^{20} m^{-3} as described in [16].

Parameter	Concentration
Initial [$HCOO^-$]	2 mM
Converted [$HCOO^-$]	1 mM
Interfacial [OH]	10-100 µM
Bulk [OH]	< 1 nM
Maximum possible converted [$HCOO^-$] (100% OH efficiency)	~ 17 mM

While a large body of work is available using indirect measurements of radicals in plasma-treated solutions, nearly all these results give at most a first indication of the relative importance of different radicals. One should be exceedingly careful before drawing any quantitative conclusions from such measurements. There is really an opportunity for our community to develop more detailed models of the underpinning transport and kinetics for the analysis of such measurement techniques. These models should consider the non-homogeneous radical densities present in plasma-liquid systems near the plasma-liquid interface. While sufficient transport and reaction rate coefficients might be available to model well-studied molecules such as formate and phenol [175], [176], this might become a challenge for more complex systems and dedicated experiments might be needed to provide mastered conditions in which these quantities can be derived with low uncertainty.

c. Near interfacial liquid phase diagnostics

As described above, many of the chemical reactions induced by plasmas in liquids are enabled by radical species near the plasma-liquid interface. The penetration depth of key species such as solvated electrons and OH radicals in water will typically not significantly exceed 1 µm. Probing this interface remains a major challenge. Furthermore, water and many other solutions are dielectrics and hence surface ionization waves, and surface charging are key processes, but the properties of the actual plasma-liquid interface have rarely if at all been directly experimentally investigated. While much work

remains to be done, in recent years, some major advances in probing the near interfacial liquid diagnostics have been made.

i. State-of-the-art

The likely first and earliest example of the measurement of line-integrated solvated electron densities at the plasma-liquid interface is reported by Go and co-workers [177]. They leveraged the absorption band of solvated electrons in the visible-near infrared of the spectrum and achieved the measurement of a weak absorbance of the order of 10^{-5}. The authors used total internal reflection absorption spectroscopy using a series of diode lasers with multiple wavelengths using a similar configuration as shown in **Fig. 18**. While this approach enabled the measurement of near interfacial solvated electrons, the technique itself is not surface specific and the spatial resolution is due to the small penetration depth of the solvated electrons. The authors carefully confirmed that the observed absorption was due to solvated electrons through the addition of scavengers to the solution. This absorption-based approach is really a fight against the detection limit. This has motivated Sasaki to explore laser-induced desolvation to detect solvated electrons in solution [178]. In this case, a laser is used to release the solvated electrons near the interface from the solution and the number of released electrons is measured by a change in the current signal. This technique was successfully applied to a solution cathode as schematically shown in **Fig. 18**. The desolvation at a liquid anode, arguably a case with abundant solvated electrons, might be difficult as the electrons once released will likely be recaptured by the electric field in the plasma and reinjected into the solution.

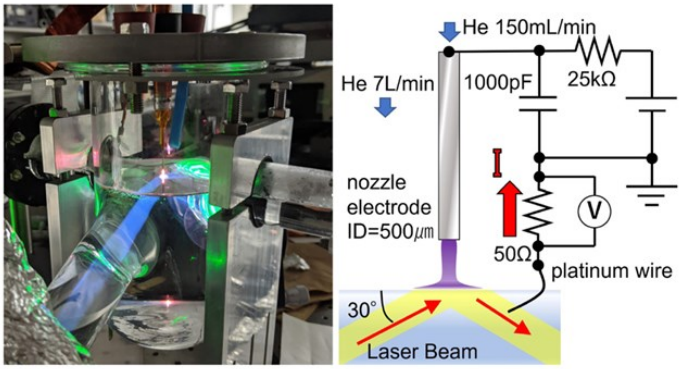

Figure 18. Experimental setup used to perform laser-induced desolvation to detect solvated electrons at the plasma liquid interface. Similar setup and laser beam configuration were used to perform total internal reflection absorption spectroscopy. Reproduced with permission from [178].

Recently, Raman scattering was applied to probe the concentrations of H_2O_2 and NO_3^- near the plasma-liquid interface by Pai [179]. He used light sheet microscopy with a spatial resolution of ~ 5 µm for concentrations in the mM range. Interestingly, interfacial layers with enhanced concentration of both species were found. These are likely the highest resolution measurements near the plasma-liquid interface reported to date. It would be exceedingly interesting to perform such measurements with higher sensitivity and further improved spatial resolution towards enabling the spatially resolved probing of also more reactive species. Fluorescent probe measurements could in principle be implemented very similarly with high resolution and potentially higher sensitivity. The near interfacial formation of radicals was for example shown through fluorescent measurements of luminol by Sasaki *et al*. [180] although without spatial resolution in the direction perpendicular to the plasma-liquid interface.

The ultimate spatial resolution to probe interfaces is of course through surface sensitive techniques such as second harmonic generation (SHG) or sum-frequency generation (SFG). To the authors knowledge only Ito *et al*. [181] reported vibrational SFG to monitor long-lived species build up at the

plasma-liquid liquid interface on minute timescales. These techniques can in principle be applied with high sensitivity and temporal resolution that would allow probing transient phenomena and short-lived species. While these techniques were already highlighted in 2016 as an opportunity for studying plasma-liquid interactions [2] further exploration remains needed.

The above approaches focused on the diagnostic to enhance the ability of probing near interfacial reactions although alternatively one could for example use thin liquid films to investigate near interfacial chemistry which we discuss in the case study below.

ii. Case study: Probing near interfacial reactions in thin liquid films

As mentioned above a canonical setup to measure plasma-liquid interactions is typically desired. One such system that not only allows us to probe near interfacial plasma-induced reactions in the liquid phase but also has significant optical access is the falling liquid film – plasma reactor as shown in **Fig. 19** . Srivastava *et al*. [182] showed that film thicknesses of a few 10s of µm are compatible with stable plasma operation. The authors found that *in situ* conversion measurements of a 1:1 ferricyanide/ferrocyanide redox mixture for thin films showed a fast likely OH-driven oxidation on < 10 ms timescales and a slow reduction on 15 ms time scales which was attributed to HO_2^-.

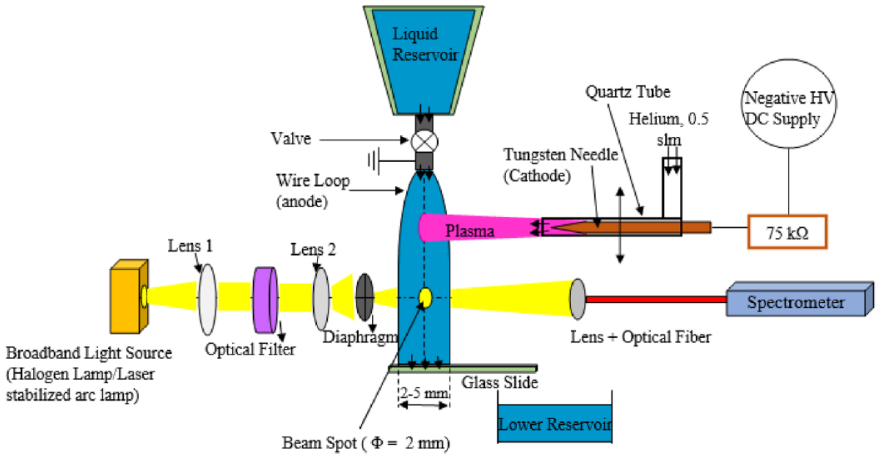

Figure 19. Schematic of a falling liquid film plasma reactor. The plasma can be vertically translated so the broadband absorption can monitor the in-situ conversion of chemical compounds on convection time scales. Reproduced with permission from [182].

A key advantage of the film is that even for absorption measurements, the signal can be dominated by near interfacial species rather than the bulk solution. Furthermore, as shown above, transport can significantly impact the analysis of liquid phase chemistry and the transport conditions in the film reactor can, at least in first approximation, be described by convection in the direction of the gravitational force and diffusion in the perpendicular direction. This allows for significant control over the often-complex transport phenomena during plasma-liquid interactions in many reactors.

6. Conclusion and opportunities

Plasma diagnostics remains exceedingly important to advance the science and applications of plasmas in and in contact with liquids. The field has made major progress in recent years, nonetheless significant opportunities exist for further development.

This includes opportunities to further refine the interpretation of OES spectra of plasmas in and in contact with liquids. This includes more detailed models for line broadening, state-to-state models for ro-vibrational di-atomic spectra and more detailed analysis of continuum radiation employing for example absolute intensities. Nonetheless such advanced models require data from the AMO (atomic,

molecular and optical physics) community that might not always be readily available. This might be an opportunity for artificial intelligence (AI) as a tool to predict spectra. Nonetheless the available data sets remain small and underpinning physics is not agreed upon which might provide a significant challenge for related AI developments

Despite significant controversy on discharge initiation, particularly in polar liquids like water, there exist a large range of experiments that have visualized key processes like electrostriction, phase change, shock waves and even electric field enhancement near electrodes. Key opportunities in this area remain to enable such measurements with both high temporal and spatial resolution on the relevant timescales of plasma initiation. Nonetheless, ultrafast ionization processes in the liquid phase remain to be investigated. While ultrafast laser-based techniques are available the key challenge remains the limited temporal resolution due to the inherent jitter in electrically initiated discharges. Potentially laser-produced plasmas in liquids might provide a pathway to investigate such ultrafast processes of interest.

In addition, there remain ample opportunities to explore and to broaden the capabilities for quantitative measurements of reactive species in both the gas and liquid phase. Diagnostics in both phases are aided by highly controlled and stabilized canonical setups that not only allow us to measure near interfacial species concentrations and properties but allow for a direct comparison with models that do not necessarily require complex transport phenomena to be included. Diagnostics in both phases can further benefit from continued developments to enhance the spatial resolution particularly near the plasma-liquid interface. LIF and TaLIF remain preferred diagnostics for temporally and spatially resolved species density measurements in the gas phase although to date have been mainly used to probe diatomic molecules like OH and atoms like O and H in the context of plasma-liquid interactions. Extending spatially resolved measurements to a broader range of reactive species of interest such as recently with the implementation of photo-fragmentation LIF imaging H_2O_2 density profiles remains of great interest [183]. In the liquid phase, a broader range of diagnostics that can probe the near interfacial liquid phase chemistry has the potential to significantly enhance our understanding of plasma-liquid interactions.

In these efforts, the community can leverage capabilities from other research fields and/or advances in diagnostic technologies. The further development of canonical systems that could be explored by different research groups with complementary expertise might be very advantageous for the continued development of the science of plasmas in and in contact with liquids. A stronger involvement of modeling in diagnostic interpretations will be beneficial. We have also highlighted a few results that are still under debate and several areas of research have not been explored extensively including the likely optical thick plasmas-in-liquids and the initial stages of discharge inception. The authors hope that this review can be a motivation factor and provide guidance in further research.

7. Acknowledgement

PJB acknowledges support from the Army Research Office under Grant No. W911NF-20-1-0105, the U.S. Department of Energy, Office of Science, Office of Fusion Energy Sciences, under award numbers DE-SC0024480 and DE-SC0020232, and the National Science Foundation under award number PHY 2020695.

Table of Contents:

This study highlights the advantages and limitations of optical diagnostics of discharges in and in contact with liquids, and includes the most recent advances in this field. Emphasis is placed on the

assumptions needed to interpret the results, which provide key information but also controversy in the interpretations that can be made of events occurring on extremely short space and time scales.

Conflict of Interest:

The authors have stated explicitly that there are no conflicts of interest in connection with this article”

The authors:

Thierry Belmonte is a CNRS research director. He was deputy director of the Institut Jean Lamour from 2009 to 2012 and then director from January 2018 to December 2022. Co-founder of a laboratory without walls with P. Choquet in Luxembourg between 2010 and 2017 on the theme of plasma-surface interaction, Thierry Belmonte works today on non-equilibrium discharges for applications in the fields of nanoparticle synthesis and materials for energy. He cosigned more than 200 publications in international peer-reviewed journals. He was awarded the Lorraine Region's first prize for research, the Jean RIST prize from the Société Française de Métallurgie et des Matériaux and the bronze medal from the CNRS.

Peter Bruggeman is a Distinguished McKnight University Professor and the Ernst Eckert Professor of Mechanical Engineering at the University of Minnesota. He currently also serves as the Director of Graduate Studies of Mechanical Engineering and the Director of the High Temperature and Plasma Laboratory. His research focuses on low temperature plasma science and engineering with applications in health and sustainability. He co-edited the 2017 and 2022 Plasma Roadmap contributing to shape research directions for the field of low temperature plasma and is founding co-organizer of the US Low Temperature Plasma Summer School. His work has been recognized by several awards including the 2018 Peter Mark Memorial Award of the American Vacuum Society, and the Inaugural 2023 University of Michigan Prize for Excellence in Plasma Science and Engineering.

References

[1] P. J. Bruggeman *et al.*, "Plasma-driven solution electrolysis," *J. Appl. Phys.*, vol. 129, no. 20, p. 200902, May 2021, doi: 10.1063/5.0044261.

[2] P. J. Bruggeman *et al.*, "Plasma–liquid interactions: a review and roadmap," *Plasma Sources Sci. Technol.*, vol. 25, no. 5, p. 053002, Sep. 2016, doi: 10.1088/0963-0252/25/5/053002.

[3] P. Vanraes and A. Bogaerts, "The essential role of the plasma sheath in plasma–liquid interaction and its applications—A perspective," *J. Appl. Phys.*, vol. 129, no. 22, p. 220901, Jun. 2021, doi: 10.1063/5.0044905.

[4] P. Bruggeman and C. Leys, "Non-thermal plasmas in and in contact with liquids," *J. Phys. Appl. Phys.*, vol. 42, no. 5, p. 053001, Mar. 2009, doi: 10.1088/0022-3727/42/5/053001.

[5] I. Adamovich *et al.*, "The 2022 Plasma Roadmap: low temperature plasma science and technology," *J. Phys. Appl. Phys.*, vol. 55, no. 37, p. 373001, Sep. 2022, doi: 10.1088/1361-6463/ac5e1c.

[6] I. Adamovich *et al.*, "The 2017 Plasma Roadmap: Low temperature plasma science and technology," *J. Phys. Appl. Phys.*, vol. 50, no. 32, p. 323001, Aug. 2017, doi: 10.1088/1361-6463/aa76f5.

[7] S. Yatom, "Diagnostics of plasma–liquids systems: Challenges and their mitigation," *Phys. Plasmas*, vol. 30, no. 3, p. 033507, Mar. 2023, doi: 10.1063/5.0139845.

[8] P. Sunka *et al.*, "Generation of chemically active species by electrical discharges in water," *Plasma Sources Sci. Technol.*, vol. 8, no. 2, pp. 258–265, May 1999, doi: 10.1088/0963-0252/8/2/006.

[9] S. Franke, R. Methling, D. Uhrlandt, R. Bianchetti, R. Gati, and M. Schwinne, "Temperature determination in copper-dominated free-burning arcs," *J. Phys. Appl. Phys.*, vol. 47, no. 1, p. 015202, Jan. 2014, doi: 10.1088/0022-3727/47/1/015202.

[10] S. Mededovic and B. R. Locke, "Primary chemical reactions in pulsed electrical discharge channels in water," *J. Phys. Appl. Phys.*, vol. 40, no. 24, pp. 7734–7746, Dec. 2007, doi: 10.1088/0022-3727/40/24/021.

[11] W. An, K. Baumung, and H. Bluhm, "Underwater streamer propagation analyzed from detailed measurements of pressure release," *J. Appl. Phys.*, vol. 101, no. 5, p. 053302, Mar. 2007, doi: 10.1063/1.2437675.

[12] K. Tachibana, Y. Takekata, Y. Mizumoto, H. Motomura, and M. Jinno, "Analysis of a pulsed discharge within single bubbles in water under synchronized conditions," *Plasma Sources Sci. Technol.*, vol. 20, no. 3, p. 034005, Jun. 2011, doi: 10.1088/0963-0252/20/3/034005.

[13] B. S. Sommers and J. E. Foster, "Plasma formation in underwater gas bubbles," *Plasma Sources Sci. Technol.*, vol. 23, no. 1, p. 015020, Feb. 2014, doi: 10.1088/0963-0252/23/1/015020.

[14] J. Wang, M. S. Simeni, M. Rong, and P. J. Bruggeman, "Absolute OH density and gas temperature measurements by laser induced fluorescence in a microsecond pulsed discharge generated in a conductive NaCl solution," *Plasma Sources Sci. Technol.*, vol. 30, no. 7, p. 075016, Jul. 2021, doi: 10.1088/1361-6595/abf71c.

[15] Stancampiano, A. *et al.*, "Plasma in interaction with water droplets," presented at the ESCAMPIG XXVI, Brno, Czech Republic, Jul. 2024.

[16] G. Oinuma, G. Nayak, Y. Du, and P. J. Bruggeman, "Controlled plasma–droplet interactions: a quantitative study of OH transfer in plasma–liquid interaction," *Plasma Sources Sci. Technol.*, vol. 29, no. 9, p. 095002, Sep. 2020, doi: 10.1088/1361-6595/aba988.

[17] Y. Yue, S. Exarhos, J. Nam, D. Lee, S. Linic, and P. J. Bruggeman, "Quantification of plasma produced OH and electron fluxes at the liquid anode and their role in plasma driven solution electrochemistry," *Plasma Sources Sci. Technol.*, vol. 31, no. 12, p. 125008, Dec. 2022, doi: 10.1088/1361-6595/acab29.

[18] Y. Yue, V. S. S. K. Kondeti, N. Sadeghi, and P. J. Bruggeman, "Plasma dynamics, instabilities and OH generation in a pulsed atmospheric pressure plasma with liquid cathode: a diagnostic

study," *Plasma Sources Sci. Technol.*, vol. 31, no. 2, p. 025008, Feb. 2022, doi: 10.1088/1361-6595/ac4b64.
[19] T. Belmonte, C. Noël, T. Gries, J. Martin, and G. Henrion, "Theoretical background of optical emission spectroscopy for analysis of atmospheric pressure plasmas," *Plasma Sources Sci. Technol.*, vol. 24, no. 6, p. 064003, Oct. 2015, doi: 10.1088/0963-0252/24/6/064003.
[20] J. Muñoz, M. S. Dimitrijević, C. Yubero, and M. D. Calzada, "Using the van der Waals broadening of spectral atomic lines to measure the gas temperature of an argon–helium microwave plasma at atmospheric pressure," *Spectrochim. Acta Part B At. Spectrosc.*, vol. 64, no. 2, pp. 167–172, Feb. 2009, doi: 10.1016/j.sab.2008.11.006.
[21] A. Y. Nikiforov, C. Leys, M. A. Gonzalez, and J. L. Walsh, "Electron density measurement in atmospheric pressure plasma jets: Stark broadening of hydrogenated and non-hydrogenated lines," *Plasma Sources Sci. Technol.*, vol. 24, no. 3, p. 034001, Apr. 2015, doi: 10.1088/0963-0252/24/3/034001.
[22] S. Iseni, C. Pichard, and A. Khacef, "Monitoring hydrodynamic effects in helium atmospheric pressure plasma jet by resonance broadening emission line," *Appl. Phys. Lett.*, vol. 115, no. 3, p. 034102, Jul. 2019, doi: 10.1063/1.5110714.
[23] P. W. Anderson, "Pressure Broadening in the Microwave and Infra-Red Regions," *Phys. Rev.*, vol. 76, no. 5, pp. 647–661, Sep. 1949, doi: 10.1103/PhysRev.76.647.
[24] P. W. Anderson, "A Method of Synthesis of the Statistical and Impact Theories of Pressure Broadening," *Phys. Rev.*, vol. 86, no. 5, pp. 809–809, Jun. 1952, doi: 10.1103/PhysRev.86.809.
[25] P. W. Anderson and Talman, J. D., "Pressure broadening of spectral lines at general pressures." Bell System Technical Publications, 1956.
[26] N. F. Allard, A. Royer, J. F. Kielkopf, and N. Feautrier, "Effect of the variation of electric-dipole moments on the shape of pressure-broadened atomic spectral lines," *Phys. Rev. A*, vol. 60, no. 2, pp. 1021–1033, Aug. 1999, doi: 10.1103/PhysRevA.60.1021.
[27] N. F. Allard, B. Deguilhem, F. X. Gadea, N. Bonifaci, and A. Denat, "Analysis of the He(3 ^{3} S)-He(2 ^{3} P) line profile obtained in dense helium plasma," *EPL Europhys. Lett.*, vol. 88, no. 5, p. 53002, Dec. 2009, doi: 10.1209/0295-5075/88/53002.
[28] N. F. Allard, B. Deguilhem, A. Monari, F. X. Gadéa, and J. F. Kielkopf, "Blue satellites on He lines due to He-He collisions," *Astron. Astrophys.*, vol. 559, p. A70, Nov. 2013, doi: 10.1051/0004-6361/201321712.
[29] N. F. Allard, N. Bonifaci, and A. Denat, "Study of the parameters of the He(3 3S)-He(2 3P) line *," *Eur. Phys. J. D*, vol. 61, no. 2, pp. 365–372, Jan. 2011, doi: 10.1140/epjd/e2010-10506-3.
[30] P. J. Leo, G. Peach, and I. B. Whittingham, "Close-coupled calculation of self-broadening of helium triplet lines," *J. Phys. B At. Mol. Opt. Phys.*, vol. 28, no. 4, pp. 591–607, Feb. 1995, doi: 10.1088/0953-4075/28/4/010.
[31] N. Bonifaci, F. Aitken, H. V. Nguyen, V. M. Atrazhev, K. V. Haeften, and R. Rincon, "Shape of atomic lines emitted by cryoplasma in Helium," *J. Phys. Conf. Ser.*, vol. 397, p. 012066, Dec. 2012, doi: 10.1088/1742-6596/397/1/012066.
[32] N. Bonifaci, F. Aitken, V. M. Atrazhev, S. L. Fiedler, and J. Eloranta, "Experimental and theoretical characterization of the long-range interaction between He * (3 s) and He(1 s)," *Phys. Rev. A*, vol. 85, no. 4, p. 042706, Apr. 2012, doi: 10.1103/PhysRevA.85.042706.
[33] H. R. Harrison, L. M. Sander, and B. E. Springett, "Electron mobility and localization in dense He ^{4} gas," *J. Phys. B At. Mol. Phys.*, vol. 6, no. 5, pp. 908–917, May 1973, doi: 10.1088/0022-3700/6/5/026.
[34] J. L. Levine and T. M. Sanders, "Mobility of Electrons in Low-Temperature Helium Gas," *Phys. Rev.*, vol. 154, no. 1, pp. 138–149, Feb. 1967, doi: 10.1103/PhysRev.154.138.
[35] J. Eloranta and V. A. Apkarian, "A time dependent density functional treatment of superfluid dynamics: Equilibration of the electron bubble in superfluid He4," *J. Chem. Phys.*, vol. 117, no. 22, pp. 10139–10150, Dec. 2002, doi: 10.1063/1.1520139.

[36] A. P. Hickman, W. Steets, and N. F. Lane, “Nature of excited helium atoms in liquid helium: A theoretical model,” *Phys. Rev. B*, vol. 12, no. 9, pp. 3705–3717, Nov. 1975, doi: 10.1103/PhysRevB.12.3705.
[37] K. Hiroike, N. R. Kestner, S. A. Rice, and J. Jortner, “Study of the Properties of an Excess Electron in Liquid Helium. II. A Refined Description of Configuration Changes in the Liquid,” *J. Chem. Phys.*, vol. 43, no. 8, pp. 2625–2632, Oct. 1965, doi: 10.1063/1.1697187.
[38] J. Jortner, N. R. Kestner, S. A. Rice, and M. H. Cohen, “Study of the Properties of an Excess Electron in Liquid Helium. I. The Nature of the Electron—Helium Interactions,” *J. Chem. Phys.*, vol. 43, no. 8, pp. 2614–2625, Oct. 1965, doi: 10.1063/1.1697186.
[39] L. Lehtovaara, T. Kiljunen, and J. Eloranta, “Efficient numerical method for simulating static and dynamic properties of superfluid helium,” *J. Comput. Phys.*, vol. 194, no. 1, pp. 78–91, Feb. 2004, doi: 10.1016/j.jcp.2003.08.020.
[40] F. Dalfovo, A. Lastri, L. Pricaupenko, S. Stringari, and J. Treiner, “Structural and dynamical properties of superfluid helium: A density-functional approach,” *Phys. Rev. B*, vol. 52, no. 2, pp. 1193–1209, Jul. 1995, doi: 10.1103/PhysRevB.52.1193.
[41] L. Lehtovaara, J. Toivanen, and J. Eloranta, “Solution of time-independent Schrödinger equation by the imaginary time propagation method,” *J. Comput. Phys.*, vol. 221, no. 1, pp. 148–157, Jan. 2007, doi: 10.1016/j.jcp.2006.06.006.
[42] L. Lehtovaara, T. Kiljunen, and J. Eloranta, “Efficient numerical method for simulating static and dynamic properties of superfluid helium,” in *CSC Report on Scientific Computing 2001–2003*, Ed. by Kotila, Haataja, Forsström, Ignatius, Jukka, Laine, Runeberg, Raback and Savolainen., vol. Chapter 20, The Finnish IT Center for Science, 2003, p. 96.
[43] P. Kepple and H. R. Griem, “Improved Stark Profile Calculations for the Hydrogen Lines H α , H β , H γ , and H δ,” *Phys. Rev.*, vol. 173, no. 1, pp. 317–325, Sep. 1968, doi: 10.1103/PhysRev.173.317.
[44] Griem, Hans R., *Spectral line broadening by plasmas*. New Yor, Academic Press, 1974.
[45] M. A. Gigosos and V. Cardeñoso, “New plasma diagnosis tables of hydrogen Stark broadening including ion dynamics,” *J. Phys. B At. Mol. Opt. Phys.*, vol. 29, no. 20, pp. 4795–4838, Oct. 1996, doi: 10.1088/0953-4075/29/20/029.
[46] S. Djurović *et al.*, “Measurements of H β Stark central asymmetry and its analysis through standard theory and computer simulations,” *Phys. Rev. E*, vol. 79, no. 4, p. 046402, Apr. 2009, doi: 10.1103/PhysRevE.79.046402.
[47] J. M. Palomares, J. Torres, M. A. Gigosos, J. J. A. M. Van Der Mullen, A. Gamero, and A. Sola, “Balmer-β Line Asymmetry Characteristics in a High Pressure, Microwave-Produced Argon Plasma,” *Appl. Spectrosc.*, vol. 63, no. 11, pp. 1223–1231, Nov. 2009, doi: 10.1366/000370209789806821.
[48] H. R. Griem and K. Y. Shen, “Stark Broadening of Hydrogenic Ion Lines in a Plasma,” *Phys. Rev.*, vol. 122, no. 5, pp. 1490–1496, Jun. 1961, doi: 10.1103/PhysRev.122.1490.
[49] M. A. Gigosos, M. Á. González, and V. Cardeñoso, “Computer simulated Balmer-alpha, -beta and -gamma Stark line profiles for non-equilibrium plasmas diagnostics,” *Spectrochim. Acta Part B At. Spectrosc.*, vol. 58, no. 8, pp. 1489–1504, Aug. 2003, doi: 10.1016/S0584-8547(03)00097-1.
[50] S. A. Flih, E. Oks, and Y. Vitel, “Comparison of the Stark widths and shifts of the H-alpha line measured in a flash tube plasma with theoretical results,” *J. Phys. B At. Mol. Opt. Phys.*, vol. 36, no. 2, pp. 283–296, Jan. 2003, doi: 10.1088/0953-4075/36/2/309.
[51] M. Ivković, N. Konjević, and Z. Pavlović, “Hydrogen Balmer beta: The separation between line peaks for plasma electron density diagnostics and self-absorption test,” *J. Quant. Spectrosc. Radiat. Transf.*, vol. 154, pp. 1–8, Mar. 2015, doi: 10.1016/j.jqsrt.2014.11.014.
[52] V. Milosavljević and G. Poparić, “Atomic spectral line free parameter deconvolution procedure,” *Phys. Rev. E*, vol. 63, no. 3, p. 036404, Feb. 2001, doi: 10.1103/PhysRevE.63.036404.

[53] D. Nikolić, S. Djurović, Z. Mijatović, R. Kobilarov, and N. Konjević, “On Modeling of the Spectral Line Shape of Heavy Neutral Nonhydrogen-Like Emitters,” *J. Appl. Spectrosc.*, vol. 68, no. 6, pp. 902–910, 2001, doi: 10.1023/A:1014326410117.
[54] D. Nikolić, S. Djurović, Z. Mijatović, and R. Kobilarov, “Comment on ‘Atomic spectral line-free parameter deconvolution procedure,’” *Phys. Rev. E*, vol. 67, no. 5, p. 058401, May 2003, doi: 10.1103/PhysRevE.67.058401.
[55] L. A. Woltz, “Quasi-static ion broadening of isolated spectral lines,” *J. Quant. Spectrosc. Radiat. Transf.*, vol. 36, no. 6, pp. 547–555, Dec. 1986, doi: 10.1016/0022-4073(86)90127-5.
[56] V. S. Burakov, E. A. Nevar, M. I. Nedel’ko, N. A. Savastenko, and N. V. Tarasenko, “Spectroscopic diagnostics for an electrical discharge plasma in a liquid,” *J. Appl. Spectrosc.*, vol. 76, no. 6, pp. 856–863, Nov. 2009, doi: 10.1007/s10812-010-9274-z.
[57] T. Belmonte, H. Kabbara, C. Noël, and R. Pflieger, “Analysis of Zn I emission lines observed during a spark discharge in liquid nitrogen for zinc nanosheet synthesis,” *Plasma Sources Sci. Technol.*, vol. 27, no. 7, p. 074004, Jul. 2018, doi: 10.1088/1361-6595/aacee2.
[58] A. V. Nominé, C. Noel, T. Gries, A. Nominé, V. A. Milichko, and T. Belmonte, “Study by Optical Spectroscopy of Bismuth Emission in a Nanosecond-Pulsed Discharge Created in Liquid Nitrogen,” *Molecules*, vol. 26, no. 23, p. 7403, Dec. 2021, doi: 10.3390/molecules26237403.
[59] K. Grosse, V. Schulz-von Der Gathen, and A. Von Keudell, “Nanosecond pulsed discharges in distilled water: I. Continuum radiation and plasma ignition,” *Plasma Sources Sci. Technol.*, vol. 29, no. 9, p. 095008, Sep. 2020, doi: 10.1088/1361-6595/aba487.
[60] T. Namihira *et al.*, “Electron Temperature and Electron Density of Underwater Pulsed Discharge Plasma Produced by Solid-State Pulsed-Power Generator,” *IEEE Trans. Plasma Sci.*, vol. 35, no. 3, pp. 614–618, Jun. 2007, doi: 10.1109/TPS.2007.896965.
[61] A. Descoeudres, C. Hollenstein, R. Demellayer, and G. Wälder, “Optical emission spectroscopy of electrical discharge machining plasma,” *J. Phys. Appl. Phys.*, vol. 37, no. 6, pp. 875–882, Mar. 2004, doi: 10.1088/0022-3727/37/6/012.
[62] A. Descoeudres, C. Hollenstein, G. Wälder, R. Demellayer, and R. Perez, “Time- and spatially-resolved characterization of electrical discharge machining plasma,” *Plasma Sources Sci. Technol.*, vol. 17, no. 2, p. 024008, May 2008, doi: 10.1088/0963-0252/17/2/024008.
[63] R. Redmer, “Physical properties of dense, low-temperature plasmas,” *Phys. Rep.*, vol. 282, no. 2–3, pp. 35–157, Apr. 1997, doi: 10.1016/S0370-1573(96)00033-6.
[64] V. E. Fortov and I. T. Iakubov, *The Physics of Non-Ideal Plasma*. WORLD SCIENTIFIC, 1999. doi: 10.1142/3634.
[65] G. A. Kobzev, I. T. Iakubov, and M. M. Popovich, Eds., *Transport and Optical Properties of Nonideal Plasma*. Boston, MA: Springer US, 1995. doi: 10.1007/978-1-4899-1066-0.
[66] W. R. Rutgers and H. W. Kalfsbeek, “Calculations and Measurements of the Dynamic Stark Effect in Hydrogen,” *Z. Für Naturforschung A*, vol. 30, no. 6–7, pp. 739–749, Jul. 1975, doi: 10.1515/zna-1975-6-705.
[67] A. Descoeudres, *Characterization of electrical discharge machining plasmas*, vol. Thèse N°3542. École Polytechnique Fédérale de Lausane, Switzerland, 2006.
[68] A. Nominé, S. C. Troughton, A. V. Nominé, G. Henrion, and T. W. Clyne, “High speed video evidence for localised discharge cascades during plasma electrolytic oxidation,” *Surf. Coat. Technol.*, vol. 269, pp. 125–130, May 2015, doi: 10.1016/j.surfcoat.2015.01.043.
[69] F. Jaspard-Mécuson *et al.*, “Tailored aluminium oxide layers by bipolar current adjustment in the Plasma Electrolytic Oxidation (PEO) process,” *Surf. Coat. Technol.*, vol. 201, no. 21, pp. 8677–8682, Aug. 2007, doi: 10.1016/j.surfcoat.2006.09.005.
[70] L. Zhu, X. Ke, J. Li, Y. Zhang, Z. Zhang, and M. Sui, “Growth mechanisms for initial stages of plasma electrolytic oxidation coating on Al,” *Surf. Interfaces*, vol. 25, p. 101186, Aug. 2021, doi: 10.1016/j.surfin.2021.101186.
[71] C. S. Dunleavy, I. O. Golosnoy, J. A. Curran, and T. W. Clyne, “Characterisation of discharge events during plasma electrolytic oxidation,” *Surf. Coat. Technol.*, vol. 203, no. 22, pp. 3410–3419, Aug. 2009, doi: 10.1016/j.surfcoat.2009.05.004.

[72] M. Aliofkhazraei *et al.*, “Review of plasma electrolytic oxidation of titanium substrates: Mechanism, properties, applications and limitations,” *Appl. Surf. Sci. Adv.*, vol. 5, p. 100121, Sep. 2021, doi: 10.1016/j.apsadv.2021.100121.
[73] R. Liu *et al.*, “Discharge behaviors during plasma electrolytic oxidation on aluminum alloy,” *Mater. Chem. Phys.*, vol. 148, no. 1–2, pp. 284–292, Nov. 2014, doi: 10.1016/j.matchemphys.2014.07.045.
[74] L. Wang, L. Chen, Z. Yan, and W. Fu, “Optical emission spectroscopy studies of discharge mechanism and plasma characteristics during plasma electrolytic oxidation of magnesium in different electrolytes,” *Surf. Coat. Technol.*, vol. 205, no. 6, pp. 1651–1658, Dec. 2010, doi: 10.1016/j.surfcoat.2010.10.022.
[75] R. O. Hussein, X. Nie, and D. O. Northwood, “A spectroscopic and microstructural study of oxide coatings produced on a Ti–6Al–4V alloy by plasma electrolytic oxidation,” *Mater. Chem. Phys.*, vol. 134, no. 1, pp. 484–492, May 2012, doi: 10.1016/j.matchemphys.2012.03.020.
[76] X.-L. Zhu *et al.*, “Origin of Two Distinct Peaks of Ice in the THz Region and Its Application for Natural Gas Hydrate Dissociation,” *J. Phys. Chem. C*, vol. 124, no. 1, pp. 1165–1170, Jan. 2020, doi: 10.1021/acs.jpcc.9b09604.
[77] J. Jovović, S. Stojadinović, N. M. Šišović, and N. Konjević, “Spectroscopic characterization of plasma during electrolytic oxidation (PEO) of aluminium,” *Surf. Coat. Technol.*, vol. 206, no. 1, pp. 24–28, Oct. 2011, doi: 10.1016/j.surfcoat.2011.06.031.
[78] S. Stojadinović, J. Jovović, M. Petković, R. Vasilić, and N. Konjević, “Spectroscopic and real-time imaging investigation of tantalum plasma electrolytic oxidation (PEO),” *Surf. Coat. Technol.*, vol. 205, no. 23–24, pp. 5406–5413, Sep. 2011, doi: 10.1016/j.surfcoat.2011.06.013.
[79] S. Stojadinović *et al.*, “Characterization of the plasma electrolytic oxidation of titanium in sodium metasilicate,” *Appl. Surf. Sci.*, vol. 265, pp. 226–233, Jan. 2013, doi: 10.1016/j.apsusc.2012.10.183.
[80] J. Jovović, S. Stojadinović, N. M. Šišović, and N. Konjević, “Spectroscopic study of plasma during electrolytic oxidation of magnesium- and aluminium-alloy,” *J. Quant. Spectrosc. Radiat. Transf.*, vol. 113, no. 15, pp. 1928–1937, Oct. 2012, doi: 10.1016/j.jqsrt.2012.06.008.
[81] J. Jovović, “Spectroscopic study of plasma during electrolytic oxidation of magnesium-aluminium alloys,” *J. Phys. Conf. Ser.*, vol. 565, p. 012013, Dec. 2014, doi: 10.1088/1742-6596/565/1/012013.
[82] H. R. Griem, *Plasma Spectroscopy*. New York: McGraw- Hill Inc, 1964.
[83] P. J. Bruggeman, N. Sadeghi, D. C. Schram, and V. Linss, “Gas temperature determination from rotational lines in non-equilibrium plasmas: a review,” *Plasma Sources Sci. Technol.*, vol. 23, no. 2, p. 023001, Apr. 2014, doi: 10.1088/0963-0252/23/2/023001.
[84] T. Carrington, “Angular Momentum Distribution and Emission Spectrum of OH (2Σ+) in the Photodissociation of H2O,” *J. Chem. Phys.*, vol. 41, no. 7, pp. 2012–2018, Oct. 1964, doi: 10.1063/1.1726197.
[85] H. Meinel and L. Krauss, “Über die besetzung der rotationszustände von oh und C2 in niederdruckplasmen,” *J. Quant. Spectrosc. Radiat. Transf.*, vol. 9, no. 3, pp. 443–460, Mar. 1969, doi: 10.1016/0022-4073(69)90038-7.
[86] C. I. M. Beenakker, F. J. D. Heer, H. B. Krop, and G. R. Möhlmann, “Dissociative excitation of water by electron impact,” *Chem. Phys.*, vol. 6, no. 3, pp. 445–454, Dec. 1974, doi: 10.1016/0301-0104(74)85028-7.
[87] P. Bruggeman, D. Schram, M. Á. González, R. Rego, M. G. Kong, and C. Leys, “Characterization of a direct dc-excited discharge in water by optical emission spectroscopy,” *Plasma Sources Sci. Technol.*, vol. 18, no. 2, p. 025017, May 2009, doi: 10.1088/0963-0252/18/2/025017.
[88] P. Bruggeman, D. C. Schram, M. G. Kong, and C. Leys, “Is the Rotational Temperature of OH(A–X) for Discharges in and in Contact with Liquids a Good Diagnostic for Determining the Gas Temperature?,” *Plasma Process. Polym.*, vol. 6, no. 11, pp. 751–762, Nov. 2009, doi: 10.1002/ppap.200950014.

[89] R. Kienle, M. P. Lee, and K. Kohse-Höinghaus, “A scaling formalism for the representation of rotational energy transfer in OH (A 2Σ+) in combustion experiments,” *Appl. Phys. B Laser Opt.*, vol. 63, no. 4, pp. 403–418, Oct. 1996, doi: 10.1007/BF01828746.
[90] M. Klíma, P. Slavíček, M. Šíra, T. Čižmár, and P. Vaněk, “HF plasma pencil and DC diaphragm discharge in liquids — diagnostics and applications,” *Czechoslov. J. Phys.*, vol. 56, no. S2, pp. B1051–B1056, Oct. 2006, doi: 10.1007/s10582-006-0325-x.
[91] Y. Du, G. Nayak, G. Oinuma, Y. Ding, Z. Peng, and P. J. Bruggeman, “Emission considering self-absorption of OH to simultaneously obtain the OH density and gas temperature: validation, non-equilibrium effects and limitations,” *Plasma Sources Sci. Technol.*, vol. 26, no. 9, p. 095007, Aug. 2017, doi: 10.1088/1361-6595/aa8688.
[92] P. Bårmann, S. Kröll, and A. Sunesson, “Spatially and temporally resolved electron density measurements in streamers in dielectric liquids,” *J. Phys. Appl. Phys.*, vol. 30, no. 5, pp. 856–863, Mar. 1997, doi: 10.1088/0022-3727/30/5/018.
[93] P. E. Frayssines, N. Bonifaci, A. Denat, and O. Lesaint, “Streamers in liquid nitrogen: characterization and spectroscopic determination of gaseous filament temperature and electron density,” *J. Phys. Appl. Phys.*, vol. 35, no. 4, pp. 369–377, Feb. 2002, doi: 10.1088/0022-3727/35/4/313.
[94] S. Ingebrigtsen, N. Bonifaci, A. Denat, and O. Lesaint, “Spectral analysis of the light emitted from streamers in chlorinated alkane and alkene liquids,” *J. Phys. Appl. Phys.*, vol. 41, no. 23, p. 235204, Dec. 2008, doi: 10.1088/0022-3727/41/23/235204.
[95] Y. Du, Z. Peng, Y. Ding, N. Sadeghi, and P. J. Bruggeman, “Is it possible to deduce the ground state OH density from relative optical emission intensities of the OH($A^2\Sigma^+ - X^2\Pi_i$) transition in atmospheric pressure non-equilibrium plasmas?—An analysis of self-absorption,” *Plasma Sources Sci. Technol.*, vol. 25, no. 4, p. 04LT02, Jul. 2016, doi: 10.1088/0963-0252/25/4/04LT02.
[96] B. P. Lavrov, A. S. Melnikov, M. Käning, and J. Röpcke, “uv continuum emission and diagnostics of hydrogen-containing nonequilibrium plasmas,” *Phys. Rev. E*, vol. 59, no. 3, pp. 3526–3543, Mar. 1999, doi: 10.1103/PhysRevE.59.3526.
[97] N. Bonifaci and A. Denat, “Spectral analysis of light emitted by prebreakdown phenomena in nonpolar liquids and gases,” *IEEE Trans. Electr. Insul.*, vol. 26, no. 4, pp. 610–614, Aug. 1991, doi: 10.1109/14.83679.
[98] A. Denat, N. Bonifaci, and M. Nur, “Spectral analysis of the light emitted by streamers in hydrocarbon liquids,” *IEEE Trans. Dielectr. Electr. Insul.*, vol. 5, no. 3, pp. 382–387, Jun. 1998, doi: 10.1109/94.689427.
[99] P. Rozga and P. Tabaka, “Comparative analysis of breakdown spectra registered using optical spectrometry technique in biodegradable ester liquids and mineral oil,” *IET Sci. Meas. Technol.*, vol. 12, no. 5, pp. 684–690, Aug. 2018, doi: 10.1049/iet-smt.2017.0229.
[100] V. Gamaleev, H. Furuta, and A. Hatta, “Generation of micro-arc discharge plasma in highly pressurized seawater,” *Appl. Phys. Lett.*, vol. 113, no. 21, p. 214102, Nov. 2018, doi: 10.1063/1.5052578.
[101] Y. A. Lebedev and V. A. Shakhatov, “Optical emission spectra of microwave discharge in different liquid hydrocarbons,” *Plasma Process. Polym.*, vol. 17, no. 8, p. 2000003, Aug. 2020, doi: 10.1002/ppap.202000003.
[102] A. Brockhinke, J. Krüger, M. Heusing, and M. Letzgus, “Measurement and simulation of rotationally-resolved chemiluminescence spectra in flames,” *Appl. Phys. B*, vol. 107, no. 3, pp. 539–549, Jun. 2012, doi: 10.1007/s00340-012-5001-1.
[103] A. Gleizes, B. Rahmani, J. J. Gonzalez, and B. Liani, “Calculation of net emission coefficient in N_2, SF_6 and SF_6-N_2 arc plasmas,” *J. Phys. Appl. Phys.*, vol. 24, no. 8, pp. 1300–1309, Aug. 1991, doi: 10.1088/0022-3727/24/8/011.
[104] V. Adineh, “Net Emission Coefficient of Plasma Excited in the Electrical Discharge Machining Through Liquid Nitrogen Dielectric Medium,” *IEEE Trans. Plasma Sci.*, vol. 40, no. 3, pp. 853–862, Mar. 2012, doi: 10.1109/TPS.2011.2182061.

[105] P. Bílek, J. Tungli, T. Hoder, M. Šimek, and Z. Bonaventura, “Electron–neutral bremsstrahlung radiation fingerprints the initial stage of nanosecond discharge in liquid water,” *Plasma Sources Sci. Technol.*, vol. 30, no. 4, p. 04LT01, Apr. 2021, doi: 10.1088/1361-6595/abef18.
[106] G. Cristoforetti *et al.*, “Local Thermodynamic Equilibrium in Laser-Induced Breakdown Spectroscopy: Beyond the McWhirter criterion,” *Spectrochim. Acta Part B At. Spectrosc.*, vol. 65, no. 1, pp. 86–95, Jan. 2010, doi: 10.1016/j.sab.2009.11.005.
[107] A. Hamdan, C. Noël, J. Ghanbaja, and T. Belmonte, “Comparison of Aluminium Nanostructures Created by Discharges in Various Dielectric Liquids,” *Plasma Chem. Plasma Process.*, vol. 34, no. 5, pp. 1101–1114, Sep. 2014, doi: 10.1007/s11090-014-9564-y.
[108] A. Hamdan *et al.*, “Plasma-surface interaction in heptane,” *J. Appl. Phys.*, vol. 113, no. 21, p. 213303, Jun. 2013, doi: 10.1063/1.4809766.
[109] Z. Song, A. Fridman, and D. Dobrynin, “Effects of liquid properties on the development of nanosecond-pulsed plasma inside of liquid: comparison of water and liquid nitrogen,” *J. Phys. Appl. Phys.*, vol. 57, no. 17, p. 175203, Apr. 2024, doi: 10.1088/1361-6463/ad211f.
[110] M. Šimek, P. Hoffer, V. Prukner, and J. Schmidt, “Disentangling dark and luminous phases of nanosecond discharges developing in liquid water,” *Plasma Sources Sci. Technol.*, vol. 29, no. 9, p. 095001, Sep. 2020, doi: 10.1088/1361-6595/abac49.
[111] T. Kawamura *et al.*, “Generation and characterization of field-emitting surface dielectric barrier discharges in liquids,” *J. Appl. Phys.*, vol. 123, no. 4, p. 043301, Jan. 2018, doi: 10.1063/1.5011445.
[112] Simeni, Luo, and Bruggeman, “On the origins of the continuum radiation of an underwater nanosecond pulsed discharge,” 2025.
[113] I. Marinov, S. Starikovskaia, and A. Rousseau, “Dynamics of plasma evolution in a nanosecond underwater discharge,” *J. Phys. Appl. Phys.*, vol. 47, no. 22, p. 224017, Jun. 2014, doi: 10.1088/0022-3727/47/22/224017.
[114] C. Miron, M. A. Bratescu, N. Saito, and O. Takai, “Time-resolved Optical Emission Spectroscopy in Water Electrical Discharges,” *Plasma Chem. Plasma Process.*, vol. 30, no. 5, pp. 619–631, Oct. 2010, doi: 10.1007/s11090-010-9248-1.
[115] Y. A. Lebedev, G. V. Krashevskaya, T. S. Batukaev, and I. L. Epstein, “Light emission from microwave discharges in liquid hydrocarbons at the initial stages of their development,” *Plasma Process. Polym.*, vol. 18, no. 10, p. 2100051, Oct. 2021, doi: 10.1002/ppap.202100051.
[116] A. Starikovskiy, Y. Yang, Y. I. Cho, and A. Fridman, “Non-equilibrium plasma in liquid water: dynamics of generation and quenching,” *Plasma Sources Sci. Technol.*, vol. 20, no. 2, p. 024003, Apr. 2011, doi: 10.1088/0963-0252/20/2/024003.
[117] A. Starikovskiy, “Pulsed Picosecond and Nanosecond Discharge Development in Liquids with Various Dielectric Permittivity Constants,” presented at the 32nd ICPIG, Iasi, Romania, Jul. 2015.
[118] D. Andre, “Conduction and breakdown initiation in dielectric liquids,” in *2011 IEEE International Conference on Dielectric Liquids*, Trondheim, Norway: IEEE, Jun. 2011, pp. 1–11. doi: 10.1109/ICDL.2011.6015495.
[119] S. E. Derenzo, T. S. Mast, H. Zaklad, and R. A. Muller, “Electron avalanche in liquid xenon,” *Phys. Rev. A*, vol. 9, no. 6, pp. 2582–2591, Jun. 1974, doi: 10.1103/PhysRevA.9.2582.
[120] A. H. Sharbaugh and P. K. Watson, “The electric strength of hexane vapor and liquid in the critical region,” *J. Appl. Phys.*, vol. 48, no. 3, pp. 943–950, Mar. 1977, doi: 10.1063/1.323713.
[121] V. M. Atrazhev, E. G. Dmitriev, and I. T. Iakubov, “The impact ionization and electrical breakdown strength for atomic and molecular liquids,” *IEEE Trans. Electr. Insul.*, vol. 26, no. 4, pp. 586–591, Aug. 1991, doi: 10.1109/14.83675.
[122] N. Bonifaci, A. Denat, and V. Atrazhev, “Ionization phenomenon in high-density gaseous and liquid argon in corona discharge experiments,” *J. Phys. Appl. Phys.*, vol. 30, no. 19, pp. 2717–2725, Oct. 1997, doi: 10.1088/0022-3727/30/19/010.
[123] V. Y. Ushakov, “Behavior of Liquids in Strong Electric Fields,” in *Impulse Breakdown of Liquids*, in Power Systems. , Berlin, Heidelberg: Springer Berlin Heidelberg, 2007, pp. 1–51. doi: 10.1007/978-3-540-72760-6_1.

[124] V. Y. Ushakov, “Physical Discharge Initiation (Ignition) Mechanisms,” in *Impulse Breakdown of Liquids*, in Power Systems. , Berlin, Heidelberg: Springer Berlin Heidelberg, 2007, pp. 319–368. doi: 10.1007/978-3-540-72760-6_7.
[125] M. F. Chaplin, “Structure and Properties of Water in its Various States,” in *Encyclopedia of Water*, 1st ed., P. Maurice, Ed., Wiley, 2019, pp. 1–19. doi: 10.1002/9781119300762.wsts0002.
[126] O. Lesaint, “Prebreakdown phenomena in liquids: propagation ‘modes’ and basic physical properties,” *J. Phys. Appl. Phys.*, vol. 49, no. 14, p. 144001, Apr. 2016, doi: 10.1088/0022-3727/49/14/144001.
[127] C. Campbell, X. Tang, Y. Sechrest, K. Fezzaa, Z. Wang, and D. Staack, “Ultrafast x-ray imaging of pulsed plasmas in water,” *Phys. Rev. Res.*, vol. 3, no. 2, p. L022021, Jun. 2021, doi: 10.1103/PhysRevResearch.3.L022021.
[128] M. M. Kuraica, N. Konjević, and I. R. Videnović, “Spectroscopic study of the cathode fall region of Grimm-type glow discharge in helium,” *Spectrochim. Acta Part B At. Spectrosc.*, vol. 52, no. 6, pp. 745–753, Jun. 1997, doi: 10.1016/S0584-8547(96)01640-0.
[129] P. Paris *et al.*, “Intensity ratio of spectral bands of nitrogen as a measure of electric field strength in plasmas,” *J. Phys. Appl. Phys.*, vol. 38, no. 21, pp. 3894–3899, Nov. 2005, doi: 10.1088/0022-3727/38/21/010.
[130] U. Czarnetzki, D. Luggenhölscher, and H. F. Döbele, “Space and time resolved electric field measurements in helium and hydrogen RF-discharges,” *Plasma Sources Sci. Technol.*, vol. 8, no. 2, pp. 230–248, May 1999, doi: 10.1088/0963-0252/8/2/004.
[131] T. Ito, K. Kobayashi, U. Czarnetzki, and S. Hamaguchi, “Rapid formation of electric field profiles in repetitively pulsed high-voltage high-pressure nanosecond discharges,” *J. Phys. Appl. Phys.*, vol. 43, no. 6, p. 062001, Feb. 2010, doi: 10.1088/0022-3727/43/6/062001.
[132] A. Dogariu, B. M. Goldberg, S. O’Byrne, and R. B. Miles, “Species-Independent Femtosecond Localized Electric Field Measurement,” *Phys. Rev. Appl.*, vol. 7, no. 2, p. 024024, Feb. 2017, doi: 10.1103/PhysRevApplied.7.024024.
[133] M. S. Simeni, E. Baratte, C. Zhang, K. Frederickson, and I. V. Adamovich, “Electric field measurements in nanosecond pulse discharges in air over liquid water surface,” *Plasma Sources Sci. Technol.*, vol. 27, no. 1, p. 015011, Jan. 2018, doi: 10.1088/1361-6595/aaa06e.
[134] K. Schoenbach, J. Kolb, S. Xiao, S. Katsuki, Y. Minamitani, and R. Joshi, “Electrical breakdown of water in microgaps,” *Plasma Sources Sci. Technol.*, vol. 17, no. 2, p. 024010, May 2008, doi: 10.1088/0963-0252/17/2/024010.
[135] C. J. C. Jordan, M. P. Coons, J. M. Herbert, and J. R. R. Verlet, “Spectroscopy and dynamics of the hydrated electron at the water/air interface,” *Nat. Commun.*, vol. 15, no. 1, p. 182, Jan. 2024, doi: 10.1038/s41467-023-44441-2.
[136] N. Sakakibara, T. Ito, K. Terashima, Y. Hakuta, and E. Miura, “Dynamics of solvated electrons during femtosecond laser-induced plasma generation in water,” *Phys. Rev. E*, vol. 102, no. 5, p. 053207, Nov. 2020, doi: 10.1103/PhysRevE.102.053207.
[137] R. A. Gottscho and V. M. Donnelly, “Optical emission actinometry and spectral line shapes in rf glow discharges,” *J. Appl. Phys.*, vol. 56, no. 2, pp. 245–250, Jul. 1984, doi: 10.1063/1.333954.
[138] G. Cunge, D. Vempaire, M. Touzeau, and N. Sadeghi, “Broadband and time-resolved absorption spectroscopy with light emitting diodes: Application to etching plasma monitoring,” *Appl. Phys. Lett.*, vol. 91, no. 23, p. 231503, Dec. 2007, doi: 10.1063/1.2822448.
[139] P. Bruggeman, G. Cunge, and N. Sadeghi, “Absolute OH density measurements by broadband UV absorption in diffuse atmospheric-pressure He–H $_2$ O RF glow discharges,” *Plasma Sources Sci. Technol.*, vol. 21, no. 3, p. 035019, Jun. 2012, doi: 10.1088/0963-0252/21/3/035019.
[140] S. G. Belostotskiy, V. M. Donnelly, D. J. Economou, and N. Sadeghi, “Spatially Resolved Measurements of Argon Metastable $(1{\rm s}_{5})$ Density in a High Pressure Microdischarge Using Diode Laser Absorption Spectroscopy,” *IEEE Trans. Plasma Sci.*, vol. 37, no. 6, pp. 852–858, Jun. 2009, doi: 10.1109/TPS.2009.2015949.

[141] N. Liu, H. Zhong, T. Y. Chen, Y. Lin, Z. Wang, and Y. Ju, “Sensitive and single-shot OH and temperature measurements by femtosecond cavity-enhanced absorption spectroscopy,” *Opt. Lett.*, vol. 47, no. 13, p. 3171, Jul. 2022, doi: 10.1364/OL.460338.
[142] G. Berden and R. Engeln, Eds., *Cavity Ring-Down Spectroscopy: Techniques and Applications*, 1st ed. Wiley, 2009. doi: 10.1002/9781444308259.
[143] Q. Xiong, Z. Yang, and P. J. Bruggeman, “Absolute OH density measurements in an atmospheric pressure dc glow discharge in air with water electrode by broadband UV absorption spectroscopy,” *J. Phys. Appl. Phys.*, vol. 48, no. 42, p. 424008, Oct. 2015, doi: 10.1088/0022-3727/48/42/424008.
[144] J. B. Schmidt *et al.*, “Femtosecond, two-photon-absorption, laser-induced-fluorescence (fs-TALIF) imaging of atomic hydrogen and oxygen in non-equilibrium plasmas,” *J. Phys. Appl. Phys.*, vol. 50, no. 1, p. 015204, Jan. 2017, doi: 10.1088/1361-6463/50/1/015204.
[145] J. B. Schmidt, B. Sands, J. Scofield, J. R. Gord, and S. Roy, “Comparison of femtosecond- and nanosecond-two-photon-absorption laser-induced fluorescence (TALIF) of atomic oxygen in atmospheric-pressure plasmas,” *Plasma Sources Sci. Technol.*, vol. 26, no. 5, p. 055004, Mar. 2017, doi: 10.1088/1361-6595/aa61be.
[146] K. Niemi, V. S. D. Gathen, and H. F. Döbele, “Absolute calibration of atomic density measurements by laser-induced fluorescence spectroscopy with two-photon excitation,” *J. Phys. Appl. Phys.*, vol. 34, no. 15, pp. 2330–2335, Aug. 2001, doi: 10.1088/0022-3727/34/15/312.
[147] A. F. H. Van Gessel, E. A. D. Carbone, P. J. Bruggeman, and J. J. A. M. Van Der Mullen, “Laser scattering on an atmospheric pressure plasma jet: disentangling Rayleigh, Raman and Thomson scattering,” *Plasma Sources Sci. Technol.*, vol. 21, no. 1, p. 015003, Feb. 2012, doi: 10.1088/0963-0252/21/1/015003.
[148] P. J. Bruggeman, F. Iza, and R. Brandenburg, “Foundations of atmospheric pressure non-equilibrium plasmas,” *Plasma Sources Sci. Technol.*, vol. 26, no. 12, p. 123002, Nov. 2017, doi: 10.1088/1361-6595/aa97af.
[149] T. Verreycken, R. Mensink, R. V. D. Horst, N. Sadeghi, and P. J. Bruggeman, “Absolute OH density measurements in the effluent of a cold atmospheric-pressure Ar–H_2O RF plasma jet in air,” *Plasma Sources Sci. Technol.*, vol. 22, no. 5, p. 055014, Aug. 2013, doi: 10.1088/0963-0252/22/5/055014.
[150] D. Riès, G. Dilecce, E. Robert, P. F. Ambrico, S. Dozias, and J.-M. Pouvesle, “LIF and fast imaging plasma jet characterization relevant for NTP biomedical applications,” *J. Phys. Appl. Phys.*, vol. 47, no. 27, p. 275401, Jul. 2014, doi: 10.1088/0022-3727/47/27/275401.
[151] Q. Yang, J.-J. Qiao, F.-L. Sun, L.-C. Wang, and Q. Xiong, “Quantitative estimation of $^{\cdot}$OH-radical density from fluorescence decay behavior near the plasma-liquid interface by incident microscopic LIF spectroscopy,” *J. Phys. Appl. Phys.*, vol. 57, no. 31, p. 31LT01, Aug. 2024, doi: 10.1088/1361-6463/ad449d.
[152] Y. Yue, J. Jiang, V. S. S. K. Kondeti, and P. J. Bruggeman, “Spatially and temporally resolved H and OH densities in a nanosecond pulsed plasma jet: an analysis of the radical generation, transport, recombination and memory effects,” *J. Phys. Appl. Phys.*, vol. 54, no. 11, p. 115202, Mar. 2021, doi: 10.1088/1361-6463/abce2a.
[153] Y. Yue and P. J. Bruggeman, “Electron density and electron temperature measurements in an atmospheric pressure plasma interacting with liquid anode,” *Plasma Sources Sci. Technol.*, vol. 31, no. 12, p. 124004, Dec. 2022, doi: 10.1088/1361-6595/aca9f6.
[154] A. M. Lietz and M. J. Kushner, “Air plasma treatment of liquid covered tissue: long timescale chemistry,” *J. Phys. Appl. Phys.*, vol. 49, no. 42, p. 425204, Oct. 2016, doi: 10.1088/0022-3727/49/42/425204.
[155] J. A. Silsby, A. Dickenson, J. L. Walsh, and M. I. Hasan, “Resolving the spatial scales of mass and heat transfer in direct plasma sources for activating liquids,” *Front. Phys.*, vol. 10, p. 1045196, Nov. 2022, doi: 10.3389/fphy.2022.1045196.

[156] M. R. Webb, F. J. Andrade, and G. M. Hieftje, “Compact Glow Discharge for the Elemental Analysis of Aqueous Samples,” *Anal. Chem.*, vol. 79, no. 20, pp. 7899–7905, Oct. 2007, doi: 10.1021/ac070789x.
[157] K. Greda, K. Swiderski, P. Jamroz, and P. Pohl, “Flowing Liquid Anode Atmospheric Pressure Glow Discharge as an Excitation Source for Optical Emission Spectrometry with the Improved Detectability of Ag, Cd, Hg, Pb, Tl, and Zn,” *Anal. Chem.*, vol. 88, no. 17, pp. 8812–8820, Sep. 2016, doi: 10.1021/acs.analchem.6b02250.
[158] T. Srivastava, A. Dogariu, A. Morozov, and P. Bruggeman, “Liquid-to-gas transfer of sodium in a liquid cathode glow discharge,” *Plasma Sources Sci. Technol.*, vol. 33, no. 7, p. 075018, Jul. 2024, doi: 10.1088/1361-6595/ad647b.
[159] R. E. Ardrey, *Liquid Chromatography – Mass Spectrometry: An Introduction*, 1st ed. in Analytical Techniques in the Sciences. Wiley, 2003. doi: 10.1002/0470867299.
[160] R. Nogueira, M. Oliveira, and W. Paterlini, “Simple and fast spectrophotometric determination of H2O2 in photo-Fenton reactions using metavanadate,” *Talanta*, vol. 66, no. 1, pp. 86–91, Mar. 2005, doi: 10.1016/j.talanta.2004.10.001.
[161] Z. Nasri, G. Bruno, S. Bekeschus, K.-D. Weltmann, T. Von Woedtke, and K. Wende, “Development of an electrochemical sensor for in-situ monitoring of reactive species produced by cold physical plasma,” *Sens. Actuators B Chem.*, vol. 326, p. 129007, Jan. 2021, doi: 10.1016/j.snb.2020.129007.
[162] H. Tresp, M. U. Hammer, J. Winter, K.-D. Weltmann, and S. Reuter, “Quantitative detection of plasma-generated radicals in liquids by electron paramagnetic resonance spectroscopy,” *J. Phys. Appl. Phys.*, vol. 46, no. 43, p. 435401, Oct. 2013, doi: 10.1088/0022-3727/46/43/435401.
[163] P. Lukes, E. Dolezalova, I. Sisrova, and M. Clupek, “Aqueous-phase chemistry and bactericidal effects from an air discharge plasma in contact with water: evidence for the formation of peroxynitrite through a pseudo-second-order post-discharge reaction of H_2O_2 and HNO_2,” *Plasma Sources Sci. Technol.*, vol. 23, no. 1, p. 015019, Feb. 2014, doi: 10.1088/0963-0252/23/1/015019.
[164] V. S. S. K. Kondeti *et al.*, “Long-lived and short-lived reactive species produced by a cold atmospheric pressure plasma jet for the inactivation of Pseudomonas aeruginosa and Staphylococcus aureus,” *Free Radic. Biol. Med.*, vol. 124, pp. 275–287, Aug. 2018, doi: 10.1016/j.freeradbiomed.2018.05.083.
[165] J.-S. Oh *et al.*, “UV–vis spectroscopy study of plasma-activated water: Dependence of the chemical composition on plasma exposure time and treatment distance,” *Jpn. J. Appl. Phys.*, vol. 57, no. 1, p. 0102B9, Jan. 2018, doi: 10.7567/JJAP.57.0102B9.
[166] M. A. Bratescu, K. Kim, and N. Saito, “Quantitative spectrochemical analysis of solution plasma in aromatic molecules,” *Plasma Process. Polym.*, vol. 16, no. 7, p. e1900012, Jul. 2019, doi: 10.1002/ppap.201900012.
[167] V. Veronico, P. Favia, F. Fracassi, R. Gristina, and E. Sardella, “Validation of colorimetric assays for hydrogen peroxide, nitrate and nitrite ions in complex plasma-treated water solutions,” *Plasma Process. Polym.*, vol. 18, no. 10, p. 2100062, Oct. 2021, doi: 10.1002/ppap.202100062.
[168] F. Tampieri, M.-P. Ginebra, and C. Canal, “Quantification of Plasma-Produced Hydroxyl Radicals in Solution and their Dependence on the pH,” *Anal. Chem.*, vol. 93, no. 8, pp. 3666–3670, Mar. 2021, doi: 10.1021/acs.analchem.0c04906.
[169] B. Myers *et al.*, “Measuring plasma-generated $^{\cdot}OH$ and O atoms in liquid using EPR spectroscopy and the non-selectivity of the HTA assay,” *J. Phys. Appl. Phys.*, vol. 54, no. 14, p. 145202, Apr. 2021, doi: 10.1088/1361-6463/abd9a6.
[170] J.-L. Clément, N. Ferré, D. Siri, H. Karoui, A. Rockenbauer, and P. Tordo, “Assignment of the EPR Spectrum of 5,5-Dimethyl-1-pyrroline *N* -Oxide (DMPO) Superoxide Spin Adduct,” *J. Org. Chem.*, vol. 70, no. 4, pp. 1198–1203, Feb. 2005, doi: 10.1021/jo048518z.
[171] F. Wang, U. Schmidhammer, J.-P. Larbre, Z. Zong, J.-L. Marignier, and M. Mostafavi, “Time-dependent yield of the hydrated electron and the hydroxyl radical in D_2O: a picosecond pulse

radiolysis study," *Phys. Chem. Chem. Phys.*, vol. 20, no. 23, pp. 15671–15679, 2018, doi: 10.1039/C8CP02276C.
[172] V. Jirásek and P. Lukeš, "Formation of reactive chlorine species in saline solution treated by non-equilibrium atmospheric pressure He/O_2 plasma jet," *Plasma Sources Sci. Technol.*, vol. 28, no. 3, p. 035015, Mar. 2019, doi: 10.1088/1361-6595/ab0930.
[173] K. Wende *et al.*, "Identification of the biologically active liquid chemistry induced by a nonthermal atmospheric pressure plasma jet," *Biointerphases*, vol. 10, no. 2, p. 029518, Jun. 2015, doi: 10.1116/1.4919710.
[174] V. Jirásek and P. Lukeš, "Competitive reactions in Cl^- solutions treated by plasma-supplied O atoms," *J. Phys. Appl. Phys.*, vol. 53, no. 50, p. 505206, Dec. 2020, doi: 10.1088/1361-6463/abb5d6.
[175] D. R. Grymonpré, A. K. Sharma, W. C. Finney, and B. R. Locke, "The role of Fenton's reaction in aqueous phase pulsed streamer corona reactors," *Chem. Eng. J.*, vol. 82, no. 1–3, pp. 189–207, Mar. 2001, doi: 10.1016/S1385-8947(00)00345-4.
[176] F. Crapulli, D. Santoro, M. R. Sasges, and A. K. Ray, "Mechanistic modeling of vacuum UV advanced oxidation process in an annular photoreactor," *Water Res.*, vol. 64, pp. 209–225, Nov. 2014, doi: 10.1016/j.watres.2014.06.048.
[177] P. Rumbach, D. M. Bartels, R. M. Sankaran, and D. B. Go, "The solvation of electrons by an atmospheric-pressure plasma," *Nat. Commun.*, vol. 6, no. 1, p. 7248, Jun. 2015, doi: 10.1038/ncomms8248.
[178] Y. Inagaki and K. Sasaki, "Detection of solvated electrons below the interface between atmospheric-pressure plasma and water by laser-induced desolvation," *Plasma Sources Sci. Technol.*, vol. 31, no. 3, p. 03LT02, Mar. 2022, doi: 10.1088/1361-6595/ac4f08.
[179] D. Z. Pai, "Plasma-liquid interfacial layer detected by in situ Raman light sheet microspectroscopy," *J. Phys. Appl. Phys.*, vol. 54, no. 35, p. 355201, Sep. 2021, doi: 10.1088/1361-6463/ac07e0.
[180] N. Shirai, G. Suga, and K. Sasaki, "Correlation between gas-phase OH density and intensity of luminol chemiluminescence in liquid interacting with atmospheric-pressure plasma," *J. Phys. Appl. Phys.*, vol. 52, no. 39, p. 39LT02, Sep. 2019, doi: 10.1088/1361-6463/ab2ff2.
[181] T. Kondo, M. Tsumaki, W. A. Diño, and T. Ito, "Influence of reactive gas-phase species on the structure of an air/water interface," *J. Phys. Appl. Phys.*, vol. 50, no. 24, p. 244002, Jun. 2017, doi: 10.1088/1361-6463/aa7159.
[182] T. Srivastava, S. Chaudhuri, C. C. Rich, G. C. Schatz, R. R. Frontiera, and P. Bruggeman, "Probing time-resolved plasma-driven solution electrochemistry in a falling liquid film plasma reactor: Identification of HO2− as a plasma-derived reducing agent," *J. Chem. Phys.*, vol. 160, no. 9, p. 094201, Mar. 2024, doi: 10.1063/5.0190348.
[183] D. Van Den Bekerom, M. M. Tahiyat, E. Huang, J. H. Frank, and T. I. Farouk, "2D-imaging of absolute OH and H_2O_2 profiles in a He–H_2O nanosecond pulsed dielectric barrier discharge by photo-fragmentation laser-induced fluorescence," *Plasma Sources Sci. Technol.*, vol. 32, no. 1, p. 015006, Jan. 2023, doi: 10.1088/1361-6595/acaa53.